



### **Science Arts & Métiers (SAM)**

is an open access repository that collects the work of Arts et Métiers Institute of Technology researchers and makes it freely available over the web where possible.

This is an author-deposited version published in: <https://sam.ensam.eu>  
Handle ID: <http://hdl.handle.net/10985/24561>

#### **To cite this version :**

Jean-Patrick GOULMY, Fabrice GUITTONNEAU, Sébastien JÉGOU, Laurent BARRALLIER -  
Classification of the acquisition conditions driving the accuracy of strain measurements during in situ DIC with scanning electron microscope - Strain - 2023

Any correspondence concerning this service should be sent to the repository

Administrator : [scienceouverte@ensam.eu](mailto:scienceouverte@ensam.eu)



**Classification of the acquisition conditions driving the accuracy of strain measurements during in-situ  
DIC with Scanning Electron Microscope**

J.P. Goulmy<sup>1</sup>, F. Guittonneau<sup>1</sup>, S. Jégou<sup>1</sup>, L. Barrallier<sup>1</sup>

<sup>1</sup> Arts et Metiers, Institute of Technology, MSMP, HESAM Université, F-13617 Aix-en-Provence, France

Corresponding author: jean-patrick.goulmy@ensam.eu (J.P. Goulmy)  
(+33) 4 42 93 82 23

**Abstract:**

Performing in-situ scanning electron microscope (SEM) tests is an interesting way to visualize strain heterogeneities under mechanical loading. An essential step before performing the tests is to define the acquisition conditions. The aim of this paper is to propose a classification of the acquisition conditions that are most important for the accuracy of strain measurements using digital image correlation (DIC) in in-situ SEM tests. More than 200 image pairs were acquired using a field emission gun SEM. The influence of different acquisition conditions was investigated: acceleration voltage, probe current, working distance, magnification, number of integrated images, image resolution, integration and number of integrated images, scan speed, contrast, brightness, and exposure time of the sample in a given area. The methodology implemented in this work is an interesting tool for detecting scan line shift, drift distortion, spatial distortion and rastering artifacts. It allows the optimization of SEM acquisition conditions for strain measurements. Finally, optimal acquisition conditions for in-situ testing are proposed and used to perform a tensile test on pure copper. The main factors highlighted include the size of the subset used in the DIC, the beam stabilization time before image acquisition, and the size of the images, which play a significant role in the results. It is recommended to apply the methodology to each device to optimize the acquisition conditions.

**Keywords:** scanning electron microscopy, Digital Image Correlation (DIC), imaging artifacts, in-situ test.

## **I. Introduction**

To determine the mechanisms of plasticity or microplasticity that lead to damage and crack initiation, digital image correlation (DIC) can be particularly useful. The use of the scanning electron microscope (SEM) is then preferred because it allows the acquisition of images at magnifications that have a resolution of less than 20 nm/pixel [1]–[3]. The quality of DIC depends on many factors [4]–[10]. One of the most important factors in the acquisition of SEM images is their stability [8], [10], [11].

It is generally accepted in the literature that four measurement artifacts occur when acquiring SEM images: Scan line shift, spatial distortion, drift distortion, and noise. According to some authors, the scan line shift artifact is related to an error in the deflection of the electron beam in the scanning coils from one scan line to another [12]. In addition, some studies show that the type of acquisition (raster scan or snake scan) could more or less favor these phenomena [13]. This artifact occurs randomly and can result in unwanted motion of random size and direction. The distortion of the electron beam is assumed to be the source of the spatial distortion artifact. This is a well-known artifact related to lens aberration, misalignment of optical elements, and lens curvature [14], [15]. This artifact is not time dependent, i.e., if you keep the same SEM acquisition parameters, it will remain constant [16]–[18]. Beam drift distortion is the result of unwanted motion of the sample relative to the electron beam while the image is acquired. This artifact is therefore not uniform in each image and varies from one image to another over time in a nonlinear manner [9]. Finally, noise artifact is also relatively present during the acquisition of successive images. It consists of a random change in the gray levels of different pixels within the image, which significantly increases the error in measuring displacement fields [10]. Unlike the other three artifacts already mentioned, it is not possible to take it into account in the calculations [10]. On the other hand, a wise choice of SEM conditions can limit its presence. Due to the systematic or random nature of these artifacts, some authors have tried to quantify their presence depending on the SEM conditions.

Through a few influential studies, authors have formulated recommendations for the SEM conditions to perform image correlations [8]–[10], [19]. However, since the SEM conditions are specific to each device, the exact definition of the conditions to be used seems difficult and a step towards better knowledge of one's device is necessary to define optimal conditions.

In addition, the number of conditions that need to be optimized in SEM is significant: electron beam voltage, beam current, working distance, type of electrons used (SE, BSE), integration mode, number of frames, scan time, acquisition time, magnification, brightness, contrast, or image resolution. The implementation of a robust methodology and the use of reliable statistical parameters is then essential to make a choice.

Several criteria have been proposed in the literature to assess the quality of images and speckle [6], [7], [20], [21]. In contrast, the precise definition of their stability using statistical criteria has been less studied. Among the criteria used is the calculation of the correlation coefficient  $C_{ZNSSD}$  (a zero-mean normalized sum of squared difference) between images, which is commonly incorporated into DIC software (Eq. 1) [22]. For a square subset with  $n = (P \times P)$  discrete pixels,  $f(x_k, y_k)$  and  $g(x'_k, y'_k)$  refer to the gray values of the  $k^{th}$  pixel of the reference and the target subset, respectively.  $\overline{f(x_k, y_k)}$  and  $\overline{g(x'_k, y'_k)}$  represent the average values of the reference and the target subset (Eq. 2).

$$C_{ZNSSD} = \sum_{k=1}^p \left[ \frac{f(x_k, y_k) - \overline{f(x_k, y_k)}}{\sqrt{\sum_{k=1}^p [f(x_k, y_k) - \overline{f(x_k, y_k)}]^2}} - \frac{g(x'_k, y'_k) - \overline{g(x'_k, y'_k)}}{\sqrt{\sum_{k=1}^p [g(x'_k, y'_k) - \overline{g(x'_k, y'_k)}]^2}} \right]^2 \quad Eq. 1$$

$$\overline{f(x_k, y_k)} = \frac{1}{p} \sum_{k=1}^p f(x_k, y_k) \text{ and } \overline{g(x'_k, y'_k)} = \frac{1}{p} \sum_{k=1}^p g(x'_k, y'_k) \quad Eq. 2$$

A value close to 0 indicates that the correlation between the two images is successful. This method is relatively efficient in detecting problems related to the arrangement of patterns on the image. On the other hand, it cannot be used to determine whether the conditions for image acquisition are stable. Other methods are based on characterization of displacement fields calculated by image correlation between two successively acquired images without load. In this case, the displacement fields are assumed to be zero. Several criteria have been proposed and it has been shown that the mean value of the displacements is of little value in determining the quality of the images. On the other hand, the calculation of the Standard Deviation of the displacements  $SD_{U_x}^{DIC}$  (e.g. defined along the  $x$ -axis) represents a first interesting criterion (Eq. 3) [19].

$$SD_{U_x}^{DIC} = \sqrt{\frac{1}{p-1} \sum_{k=1}^p |U_{x_p} - \overline{U_x}|^2} \quad Eq. 3$$

Where  $U_{xp}$  denotes a displacement value of pixel  $p$ ,  $\overline{U_x}$  represents the average value of the displacements, and  $p$  represents the number of values determined. The Relative Standard Deviation of the displacements  $RSD^{DIC}$  is then calculated after normalizing  $SD^{DIC}$  with the image size. As the standard deviation increases, the images become less similar, calling into question the quality of the image. However, this criterion is rather inadequate because it does not indicate whether the difference between the two images is due to a known measurement artifact or a random aspect.

Mansilla *et al.* have shown that both random and nonrandom measurement artifacts can lead to similar standard deviation values. Therefore, they proposed two new criteria,  $R$  and  $SC$ , to analyze instabilities in SEM images [8]. The parameter  $R$  represents the ratio between the average of the standard deviation of displacements in an image by columns ( $\overline{SD}^{cols}$ ) and rows ( $\overline{SD}^{rows}$ ) for both  $x$  and  $y$  directions. This criterion defines whether there is a preferred artifact along a given direction and can be calculated from the displacement fields  $U_x$  and  $U_y$ . Calculation examples are given for  $U_x$  (Eq. 4) and (Eq. 5).  $n$  and  $m$  are the number of rows and columns respectively.  $i$  and  $j$  refers to row and column index, respectively. With this notation,  $U_{xi}(j)$  refers to the displacement along the  $x$ -axis of the pixel at position  $(i,j)$  in the image and  $\overline{U_{xi}(j)}$  refers to the average of the displacements along the  $x$ -axis of column  $j$ .

$$\overline{SD}_{U_x}^{cols} = \frac{1}{m} \sum_{j=1}^m SD_j = \frac{1}{m} \sum_{j=1}^m \sqrt{\frac{1}{n-1} \sum_{i=1}^n (U_{xi}(j) - \overline{U_{xi}(j)})^2} \quad \text{Eq. 4}$$

$$\overline{SD}_{U_x}^{rows} = \frac{1}{n} \sum_{i=1}^n SD_i = \frac{1}{n} \sum_{i=1}^n \sqrt{\frac{1}{m-1} \sum_{j=1}^m (U_{xj}(i) - \overline{U_{xj}(i)})^2} \quad \text{Eq. 5}$$

The ratio  $R$  is defined as :

$$R = \frac{\overline{SD}^{cols}}{\overline{SD}^{rows}} \quad \text{Eq. 6}$$

When  $R$  is less than 1, a better correlation in the columns than in the rows is obtained. Conversely, when  $R$  is greater than 1, the correlation is better in the rows than in the columns. Finally, when  $R$  is close to 1, no direction is preferred. An  $R$  ratio close to 1 does not mean that the artifact is random.

To determine whether a measurement artifact is random or not, the Self-Correlation coefficient  $SC$  can be calculated from the displacement image matrix  $f(x,y)$  [23]. The method consists of convolving the image with the same image shifted by a distance  $k_1$  and  $k_2$  along  $x$  and  $y$  with respect to the center of the image. The result is a correlation matrix  $G(k_1, k_2)$  (Eq. 7). Then, the  $SC$  coefficient is calculated as a normalized correlation matrix (Eq. 8).

$$G(k_1, k_2) = \sum_{x,y} f(x,y) f(x + k_1, y + k_2) \quad \text{Eq. 7}$$

$$SC = \frac{\sum_{x,y} f(x,y) f(x + k_1, y + k_2)}{\sqrt{\sum_{x,y} f(x,y)^2 \sum_{x,y} f(x + k_1, y + k_2)^2}} \quad \text{Eq. 8}$$

The more equal the displacement image matrix and the shifted displacement image matrix are, the higher the value of the  $SC$  coefficient. By definition,  $SC$  is maximal (equal to 1) for a displacement vector  $(k_1, k_2) = (0, 0)$ , i.e., for

two identical images with not relative displacement. Since the  $SC$  coefficient is calculated for each pixel of the displacement image matrix, a map characteristic of the periodicity of the displacement fields is obtained. The obtained circles or color bands can be interpreted in terms of measurement artifacts related to the SEM acquisition parameters. Finally, an Average  $AV^{SC}$  and a Standard Deviation  $SD^{SC}$  can be calculated for each  $SC$  map. The  $SD^{SC}$  parameter is used to calculate the standard deviation around the  $AV^{SC}$  average. For example, if  $AV^{SC}$  is close to 0 and the  $SD^{SC}$  parameter is low, this indicates the absence of artifact or the presence of a random artifact.

On the other hand, this parameter cannot be used to determine the amplitude of randomness. For this purpose, the calculation of the Relative Standard Deviation of displacements  $RSD^{DIC}$  is useful. To date, this method seems to be the most robust for assessing the presence of artifacts in the acquisition of SEM images.

The SEM conditions to be optimized are numerous and the optimal conditions depend on each device. It now seems appropriate to propose a classification of the parameters that have the greatest influence on the results of the previously mentioned statistical parameters. To our knowledge, no extended study concerning the influence of the SEM parameters has yet been conducted using a single methodology. Although the influence of many acquisition parameters has already been investigated in the literature [8], [18], [19], the studies performed were generally limited to a restricted number of acquisition parameters [8] and/or the use of a statistical parameter specific to each study to quantify the quality of the images [18], [19]. Therefore, it is difficult to provide a classification of the influence of the SEM acquisition parameters on the presence of measurement artifacts.

This classification could help to identify the parameters to focus on in order to improve the quality of acquisitions. Moreover, with the previously presented method, it is not possible to evaluate the presence of spatial artifacts, since they are constant from one image to another when no shift is applied. Therefore, it is proposed to modify the methodology to detect and account for the presence of spatial artifacts. In addition, special attention has been paid to the influence of the size of the subsets used in DIC and to temporal phenomena that have been least discussed in the literature. The use of autocorrelation mappings and the combination of several statistical parameters were also considered. Finally, a mechanical test was performed to demonstrate the success of the methodology.

## II. Materials and methods

Prior to image acquisition, speckle was dropped onto the surface of the steel material after mirror diamond polishing down to 1  $\mu\text{m}$  and then chemically etched with a 3% Nital solution (nitric acid in ethanol). A drop of an  $\text{Al}_2\text{O}_3$  pH 8.5 solution diluted in acetone was then dropped onto the surface of the specimens and dried with an air dryer. This procedure was then repeated to achieve the desired density of speckle.

After binarizing the images using the Otsu method [24], the speckle density was defined as the ratio between the number of white pixels and the total number of pixels. Speckle density was found to be between 0.39 and 0.58. The speckle density was therefore considered to be sufficiently repeatable on the surface of the sample to neglect its influence on the results. The influence of the speckle quality on the results will be discussed in section IV. 2. Images were acquired using the SEM-FEG JEOL JSM-7001F in High Vacuum mode (HV). A pair of images was acquired consecutively under the same conditions with a minimum interval of one minute between each image. Each measurement condition was repeated more than three times at different daily intervals. The average values and the standard deviations of the individual values are shown in the graphs. In all, more than 200 image pairs were acquired. Unless otherwise stated in the text, the standard acquisition conditions are defined in Table 1. Of these conditions, only one parameter was changed each time.

Acceleration voltage (kV)	Probe current number	Objective lens aperture	Working distance (mm)	Image size (px <sup>2</sup> )	Integration	Number of frames	Scan time number	Dwell time ( $\mu\text{s}$ )	Magnification	Resolution (nm/pixel)
10	9	3 (50 $\mu\text{m}$ )	13	1280 $\times$ 1056	yes	4	5	2.89	$\times$ 1500	63

**Table 1. Standard acquisition conditions.**

The results reported in the literature having been obtained on different SEMs, it was considered interesting to establish a consistent test matrix to characterize a maximum of acquisition parameters.

- An increase in the acceleration voltage generally leads to: a decrease in secondary emission yields, an unchanged compositional contrast, high charges, a low contamination [25]. It was therefore expected that this parameter had little or no influence on the results. Commonly used acceleration voltages in the literature were therefore used: 5 kV, 10 kV and 15 kV.

- The acquisition time is difficult to dissociate from the scan time or dwell time. According to Sutton *et al.* a decrease in dwell time on a pixel leads to an increase in noise [18]. At the same time, limiting the image acquisition time to limit the measurement of artifacts is recommended [8]. A compromise must therefore be found between a sufficiently long dwell time to limit noise on the images and a sufficiently short dwell time to limit artifacts and in particular beam drift distortion, which evolves with time. The scan time

number was set as follows: 1, 3, 5, 7, and 9. Note that the scan number is a JEOL-specific setting, the corresponding dwell time are 0.22, 0.76, 2.89, 14.80 and 61.67  $\mu\text{s}$  respectively.

- Image integration can reduce measurement artifacts and noise [10], [18], [19]. Furthermore, an increase in the number of frames to integrate images drastically decreases measurement artifacts [8], [18]. Mansilla *et al.* stated, however, that relatively identical or nearly identical results are obtained if the dwell time is adjusted to have the same acquisition time [8]. Images were taken under similar conditions with or without integration. The number of integrated images ranged from 2, 4, 8, 16, and 32.

- It was observed by Sutton *et al.* that the standard deviation of the strain measurements increases as the magnification increases. The artifact is then attributed to beam distortion [9], [18]. In this work, the magnifications used were  $\times 500$ ,  $\times 1500$ , and  $\times 5000$ . Under the selected conditions, the pixel sizes obtained were 189, 63, and 19 nm respectively when the image size was  $1280 \times 1056$  pixels. The horizontal field of view corresponding to each magnification is equal to 242, 80 and 24.2  $\mu\text{m}$  respectively.

- An increase in probe current generally leads to: better image quality, unchanged resolution, high secondary emission, high sample contamination, large recommended aperture size, and low condenser current. The aperture of the diaphragm was set to 50  $\mu\text{m}$ . Its influence was not investigated. The probe current number was fixed at: 7, 8, 9, 10, 11. For an acceleration voltage of 15 kV and an aperture of the diaphragm of 50  $\mu\text{m}$ , these values correspond to 0.1, 0.3, 0.5, 0.7, 1 nA respectively.

- According to Sutton *et al.* the smaller the working distance the more scan line shift artifact is observed. In addition, working distance also has an impact on the presence of spatial distortion artifact [18]. However, this artifact decreases with an increase in working distance. The purpose of the analysis is to carry out strain measurements during in-situ mechanical loading (not addressed in the present paper) using a dedicated Kammrath & Weiss GmbH machine. According to its 13 mm minimal working distance required, the value was therefore set between 13 and 17 mm in steps of 1 mm in order to define the optimal parameters for the acquisition of images.

- The influence of the image size was also investigated. Several authors agree that a decrease in resolution implies a decrease in artifacts. This is related to the image acquisition time. The higher the resolution of the image, the longer the acquisition time, which leads to a decrease in image stability and an increase in artifacts, particularly that of beam drift over time. High resolution images are therefore not recommended for image correlation measurements [8]. In cases where high resolution is required, then image stitching may be preferable [26]. Four image sizes were investigated:  $800 \times 600$ ,  $1280 \times 1056$ ,  $2560 \times 2048$ , and  $5120 \times 4096$  pixels, leading to resolutions of 100, 63, 31, and 16 nm/pixel respectively for a  $\times 1500$  magnification and a working distance of 13 mm.



- The synchronization mode which aims to synchronize the scanning process with the frequency of the power line was not recommended in literature and was not specifically studied in this work [8].

- The impact of the time between images was evaluated by applying an increasing interval between image capture. The choice of detector is highly dependent on the type of marker used. In the presence of markers whose atomic number is very different from the matrix of the material, the acquisition of images with the Back-Scattered Electron (BSE) detector can be particularly interesting. However, this mode introduces a significant noise in the images, leading to the preferential use of the Secondary Electron (SE) detector. In the case of this work, alumina was applied to the surface of the samples to serve as speckle. Since the alumina used was relatively pure, the atomic number was constant and the speckle appeared uniformly in BSE image acquisitions (in dark grey on the image Figure 1.b). The speckle used here was therefore not suitable for BSE acquisition. All the images were acquired in SE mode.

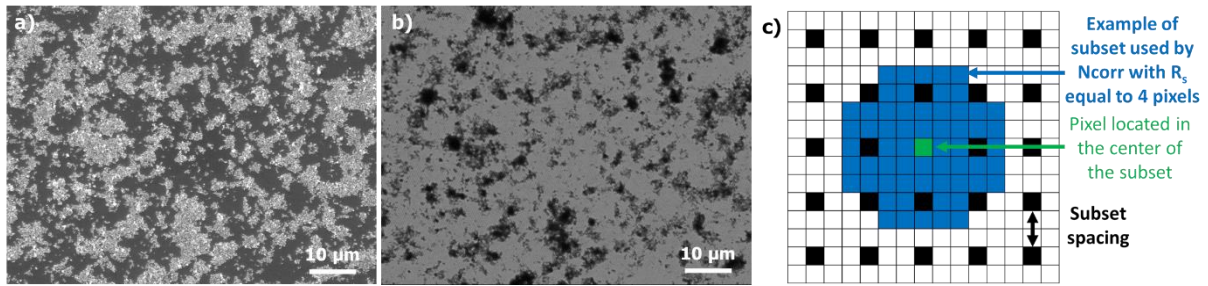


**Figure 1.** Example of images obtained with: a) SE detector, b) BSE detector. c) Definition of a subset used in DIC.

The *Ncorr vers. 1.2* was used to correlate the images [27]. The pixel spacing was arbitrarily set to 2 pixels. The calculation of displacements is therefore only performed every two pixels of the image (Figure 1.c). The subsets used to calculate the displacements are circular in shape. To evaluate the influence of the subset size, three values of radius subset  $R_s$  were investigated: 15, 30 and 60 pixels. Due to the direction of the beam scan, some SEM conditions induce more stable conditions in a given direction [28]. To evaluate this point, displacement fields are calculated in both  $x$  (horizontal) and  $y$  (vertical) directions. Following the obtaining of the displacement fields, the criteria  $RSD^{DIC}$ ,  $R$ ,  $AV^{SC}$ ,  $SD^{SC}$ , introduced in section I, were calculated for each direction. Ranges of acceptance (depicted by colored areas on the graphs) were defined to determine if an image was of sufficient quality and stability. This choice was made according to the results obtained and the recommendations given by Mansilla *et al.* [8]. The selected values as well as the color codes associated with each criterion are defined in Table 2.

	$RSD^{DIC}$	$R$	$AV^{SC}$	$SD^{SC}$	$C_{ZNSSD}$
Minimum value	0	0.9	-0.025	0	0
Maximum value	$0.3 \cdot 10^5$	1.1	0.025	0.125	0.2

**Table 2.** Ranges of acceptance for the statistical parameters in case of stain measurement.

### III. Results

#### III. 1. Influence of subset radius $R_s$ used in DIC

Before addressing the influence of SEM acquisition parameters, the influence of the subset radius  $R_s$  used in DIC is evaluated in Figure 2. Three acceleration voltages were investigated, the other acquisition conditions were fixed in Table 1. The same trends for the three voltages are observed. An increase in the subset radius  $R_s$  leads to a decrease in the statistical parameters  $RSD^{DIC}$  and  $C_{ZNSSD}$ . In fact, the use of low subset radius  $R_s$  generates significant random noise on the displacement fields [29]. At the same time, the statistical parameters  $R$ ,  $AV^{SC}$  and  $SD^{SC}$  are increased in most cases. By their definition, the parameters  $R$ ,  $AV^{SC}$  and  $SD^{SC}$  are sensitive to the randomness of the displacement fields. The more random the displacement field, the closer the values of these parameters are to 0. Thus, the presence of noise in the image, increases the randomness and drastically reduces the values of  $R$ ,  $AV^{SC}$  and  $SD^{SC}$ . Thus, the presence of artifacts of scan line shift or drift distortion can be hidden. By decreasing the noise by increasing the subset radius  $R_s$ , the value of the parameters  $R$ ,  $AV^{SC}$  and  $SD^{SC}$  increase and are then more sensitive to scan line shift and drift distortion artifacts.

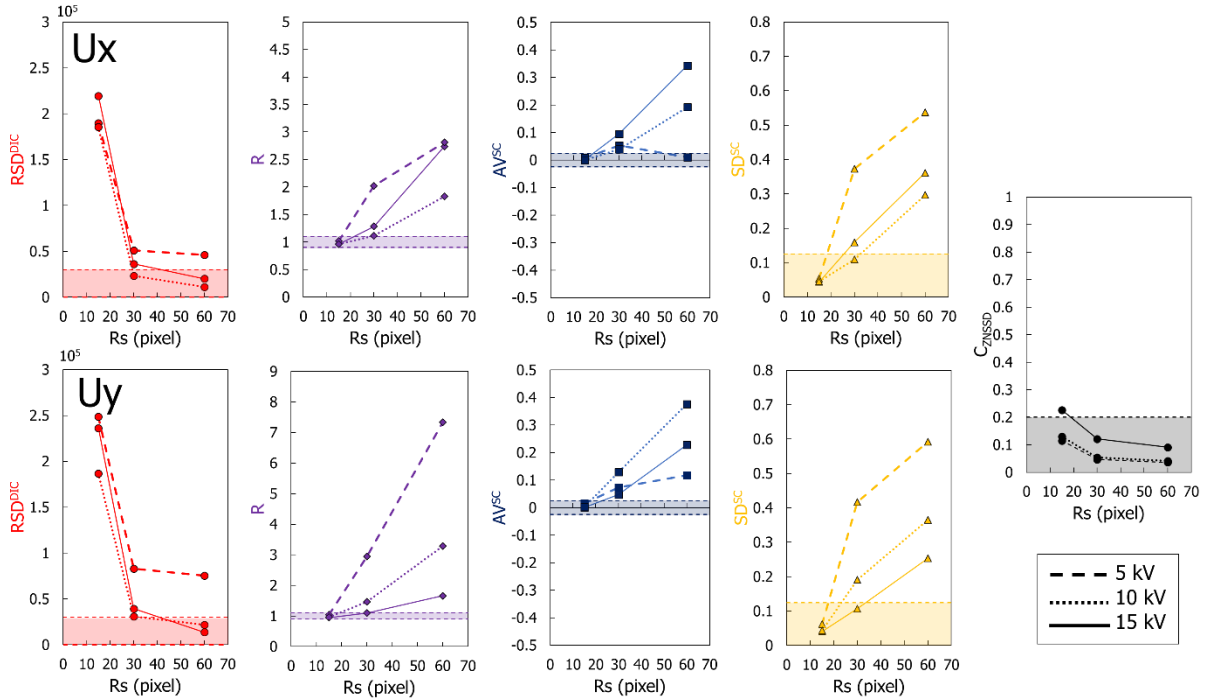


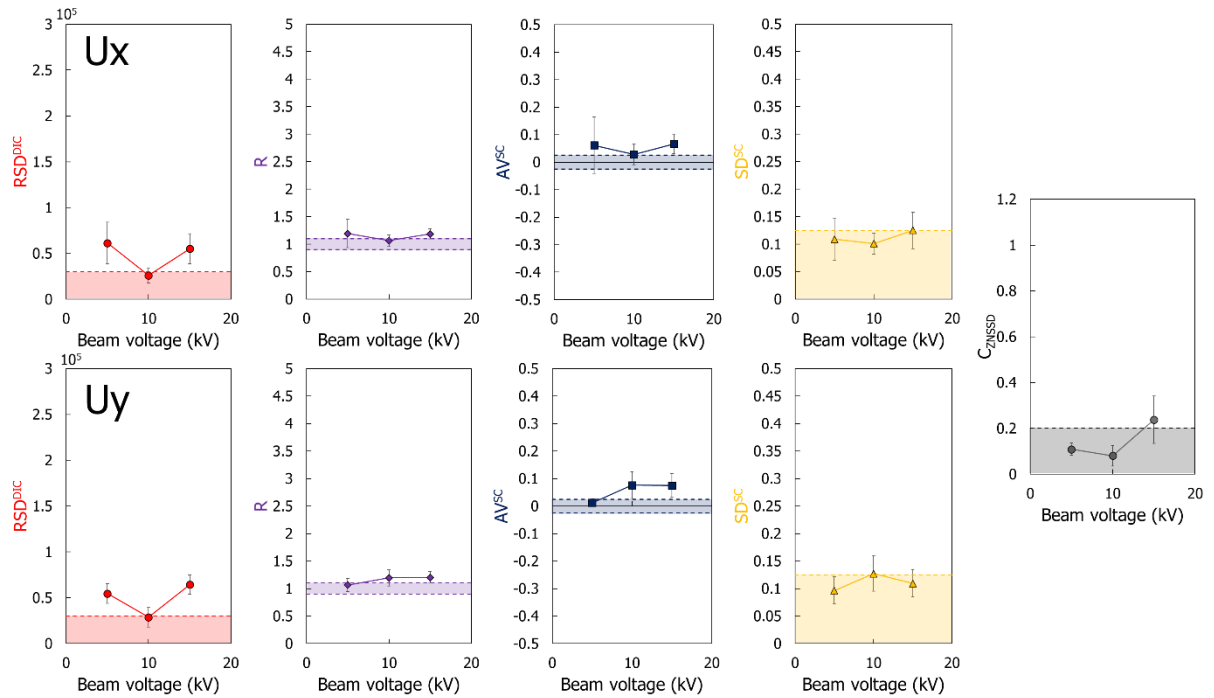
**Figure 2. Evolution of statistical parameters as a function of subset size  $R_s$ . Investigated acceleration voltage: 5, 10 and 15 kV. Probe current number: 9, working distance: 13 mm, image size 1280×1056 pixels, integration: yes, number of frames: 4, scan time number: 5, mode: SE, magnification: ×1500. The colored area corresponds to the range of validity of each parameter defined in Table 2.**

It is therefore necessary to set the subset size of the study beforehand to select the optimal SEM conditions. The use of a subset radius  $R_s$  too small will not allow us to determine the presence of measurement artifacts ( $R_s = 15$ ) with the statistical parameters used according to the considerations made just above. It should therefore be avoided.

On the other hand, increasing the value of  $R_s$  allows for more effective detection of the presence of artifacts. However, if a line shift artifact appears during the acquisition, it will be less visible due to the averaging of the displacement fields. An intermediate value is therefore desirable to optimize the acquisition conditions. In the following, the  $R_s$  is set to 30 pixels (i.e. 1.9  $\mu\text{m}$ ).

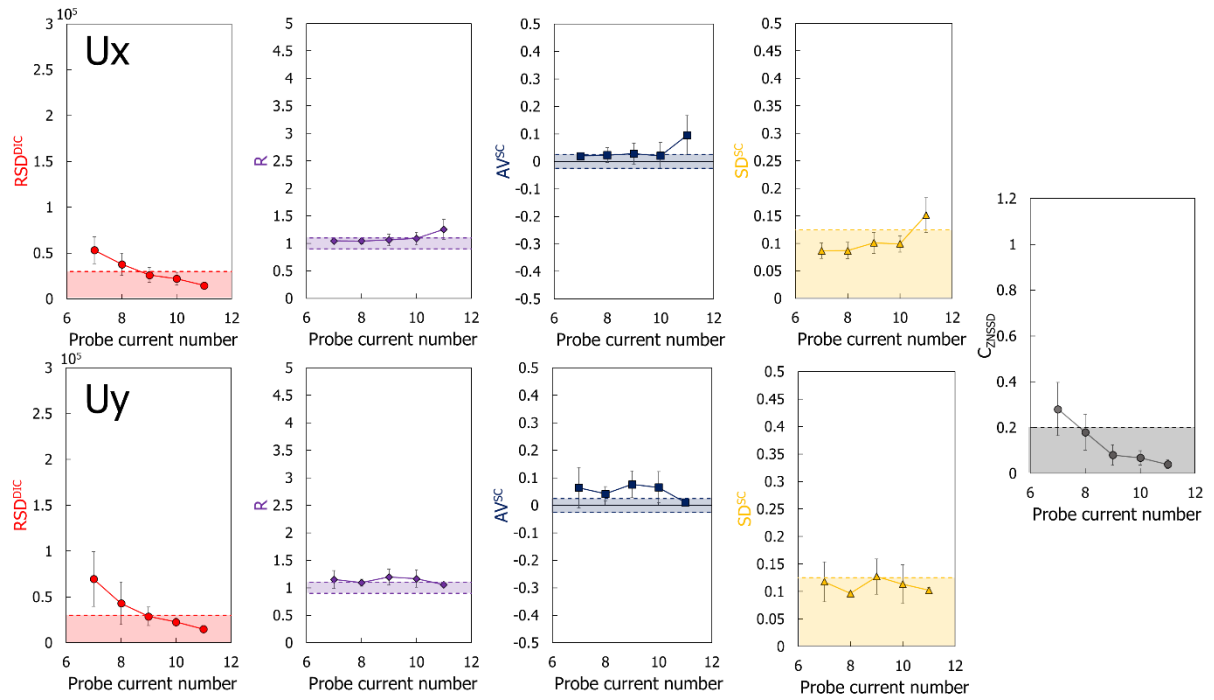
### III. 2. Influence of SEM acquisition parameters

Figure 3 shows the results obtained concerning the influence of the acceleration voltage. As expected, the impact does not appear to be very strong. Although the results are interesting at 15 kV, high acceleration voltage can contaminate or damage the surfaces of many materials and can affect the quality of the speckle pattern if multiple scans are required. It is therefore advisable to limit the use of this value. For the lowest voltage (5 kV), although the mean values are close to the ranges set for all statistical parameters, the standard deviation is higher than for the other conditions. The DIC quality then becomes more arbitrary at this condition. It is therefore to be avoided. Under these conditions, the combined set of criteria indicate that the most adequate condition among those used is an acceleration voltage of 10 kV.



**Figure 3. Evolution of the statistical parameters as a function of the acceleration voltage, magnification  $\times 1500$ . Two acquisitions. Probe current number: 9, working distance: 13 mm, image size  $1280 \times 1056$  pixels, integration: yes, number of frames: 4, scan time number: 5, mode: SE, magnification:  $\times 1500$ . The colored area corresponds to the range of validity of each parameter defined in Table 2.**

The influence of the probe current value on the statistical parameters is shown in Figure 4. The impact of this parameter is limited. The evolution is similar for the parameters  $RSD^{DIC}$  and  $C_{ZNSSD}$  with a decrease when the probe current increases. These results are in agreement with the observations made by Kammers *et al.* indicating that an increase in the spot size generally decreases the noise in the images [19]. From a probe current number equal to 9, these two parameters belong to the ranges that guarantee a quality image. The  $R$  parameter is relatively constant with the value of probe current. Finally, the  $AV^{SC}$  and  $SD^{SC}$  parameters evolve in a similar way and are within the set criteria except for a value of 11 for  $U_x$  displacements. The optimal measurement conditions are therefore located at probe current number 9.



**Figure 4. Evolution of statistical parameters as a function of the probe current. Acceleration voltage: 10 kV, working distance: 13 mm, image size 1280×1056 pixels, integration: yes, number of frames: 4, scan time number: 5, mode: SE, magnification: ×1500. The colored area corresponds to the range of validity of each parameter defined in Table 2.**

Figure 5 shows the evolution of the statistical parameters as a function of the scan time parameter for images integrated 4 times (dashed lines) and not integrated (solid lines). We recall here that the higher the scan time parameter, the longer the acquisition time. The trends are similar for integrated and non-integrated images. For scan time lower than 5 (dwell time of 2.89  $\mu$ s), the correlation coefficient  $C_{ZNSSD}$  is higher than the range set. The image quality is not sufficiently good to interpret the other statistical parameters. For scan time higher than 5, a clear increase in  $R$  and  $SD^{SC}$  values is observed. For the highest scan time 9 (dwell time of 61.67  $\mu$ s), the relative standard deviation of displacements  $RSD^{DIC}$  increases sharply for the non-integrated images. The evolution of the  $AV^{SC}$  parameter is more difficult to comment on with unstable values as a function of the scan time parameter. The

condition that limits the presence of artifact is obtained with a scan time of 5 in the case where the images are integrated. Scan time 5 also appears to be the best when the images are not integrated. It is obvious that for all statistical parameters, the use of image integration is beneficial, which confirms the results previously obtained in the literature [10], [18], [19]. The benefit, on the other hand, varies depending on the scan time. For extreme scan time, the benefit is large, while it is more moderate for the scan time of 5 (dwell time of 2.89  $\mu$ s).

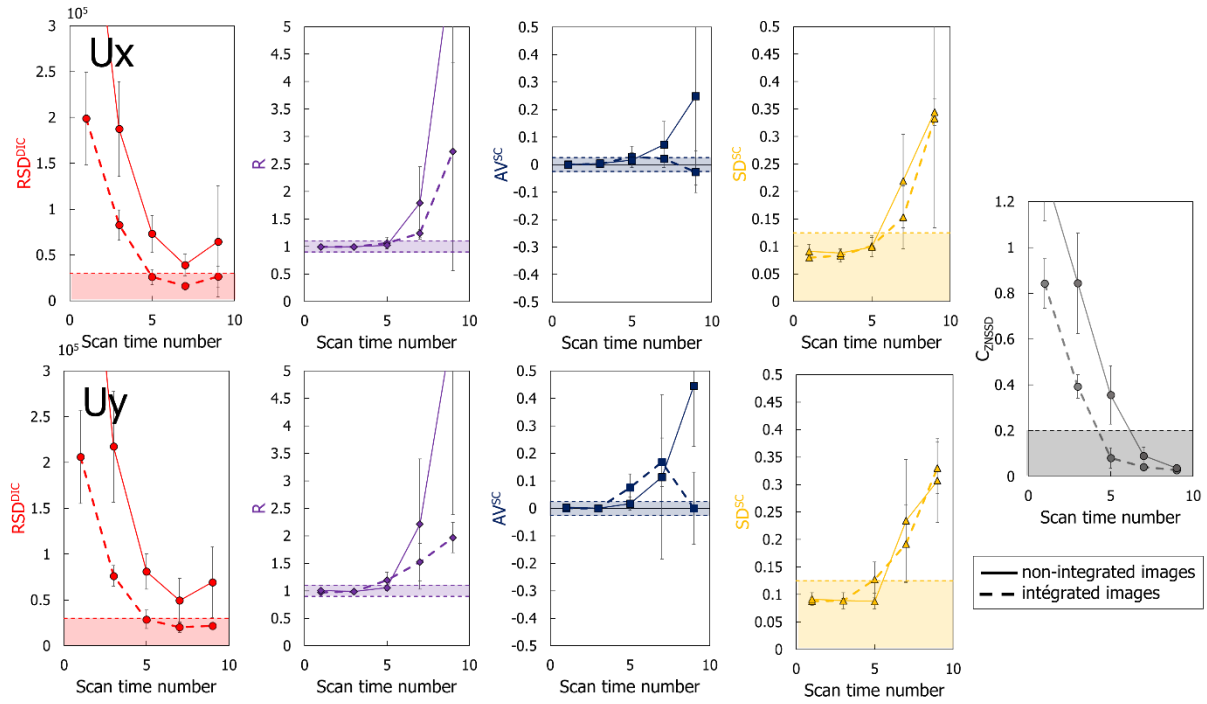


**Figure 5.** Evolution of statistical parameters as a function of scan time number; solid line represent non-integrated images; dashed line are integrated images. Acceleration voltage: 10 kV, probe current number: 9, working distance: 13 mm, image size 1280×1056 pixels, integration: yes, number of frames: 4, mode: SE, magnification: ×1500. The colored area corresponds to the range of validity of each parameter defined in Table 2.

Figure 6 shows the evolution of the statistical parameters as a function of the number of frames. The evolution is similar for all statistical parameters. A decrease is observed between 2 and 4 integrated images. Beyond that, the statistical parameters  $R$ ,  $AV^{SC}$ , and  $SD^{SC}$  are stable, while the parameters  $RSD^{DIC}$  and  $C_{ZNSSD}$  continue to decrease somewhat. An increase in the number of integrated images therefore improves their quality. These results are in agreement with those previously observed in the literature [8], [18]. Artifacts such as scan line shift and drift distortion appear randomly on the images. Since the benefits are relatively low beyond 8 integrated images, it does not seem relevant to use an integration greater than 8 images.

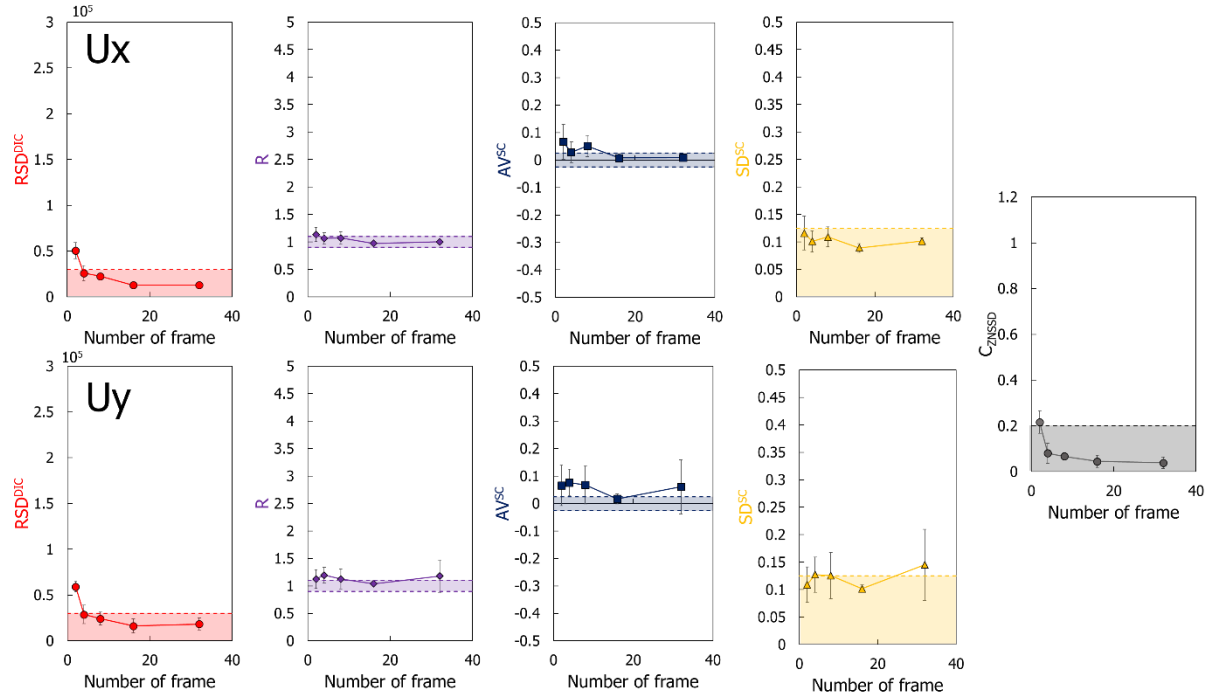


**Figure 6.** Evolution of statistical parameters as a function of number of frames. Acceleration voltage: 10 kV, probe current number: 9, working distance: 13 mm, image size 1280×1056 pixels, integration: yes, scan time number: 5, mode: SE, magnification: ×1500. The colored area corresponds to the range of validity of each parameter defined in Table 2.

The evolution of the statistical parameters as a function of the working distance is shown in Figure 7. Except for the working distance of 16 mm, the statistical parameters are stable as a function of the working distance, indicating a weak influence of this parameter (in the selected range) on the field measurements. An increase in the standard deviation for all statistical parameters is observed. To evaluate what kind of artifact can be at the origin of the results obtained for a working distance equal to 16 mm, the displacement and autocorrelation mappings are shown in Figure 8 for two acquisitions. A similar signature is obtained. Wide bands, oriented horizontally, are observed on the  $SC$  maps. In addition, one or more bands, with higher intensities, are also observed within the latter. These signatures are characteristic of the presence of line shifts in the images. The width of the bands is then characteristic of the position of the line shift in the image. The smaller the width, the more the line shift is located in the center of the image. The difference in width between the different  $SC$  mappings thus indicates that the position of the line shift is different from one image to another, confirming the randomness of the line shift artifact. The presence of several sustained bands, as observed for acquisition 2 ( $SC_{Uy}$  mapping), is characteristic of the presence of several line shifts. These line shifts are particularly visible on the  $Uy$  displacement mapping of the acquisition 2. As previously mentioned, this artifact has already been commonly observed in the literature. It occurs at the beginning of the line, when the beam is deviated during the acquisition of images. On the other hand, a deviation of the beam along the  $x$ -axis, as seen in the two acquisitions, is less common. It was previously observed by Lenthe *et al.* who explain that this artifact is more difficult to detect because the implemented raster scanning method produces

global shifts that affect all features during imaging. This artifact is thought to be related to the slow electron beam deflection and detector latency, which result in a large system response time relative to the sampling rate [13]. Moreover, the fact that this artifact occurs at a working distance of 16 mm in particular is quite surprising. It was not possible to find an explanation for this phenomenon, but it clearly demonstrates the interest of the methodology implemented here. Although influence studies allow us to define the global impact of the different parameters on the stability of the images, a verification of the analysis conditions is still necessary when the objective is to apply DIC measurements.

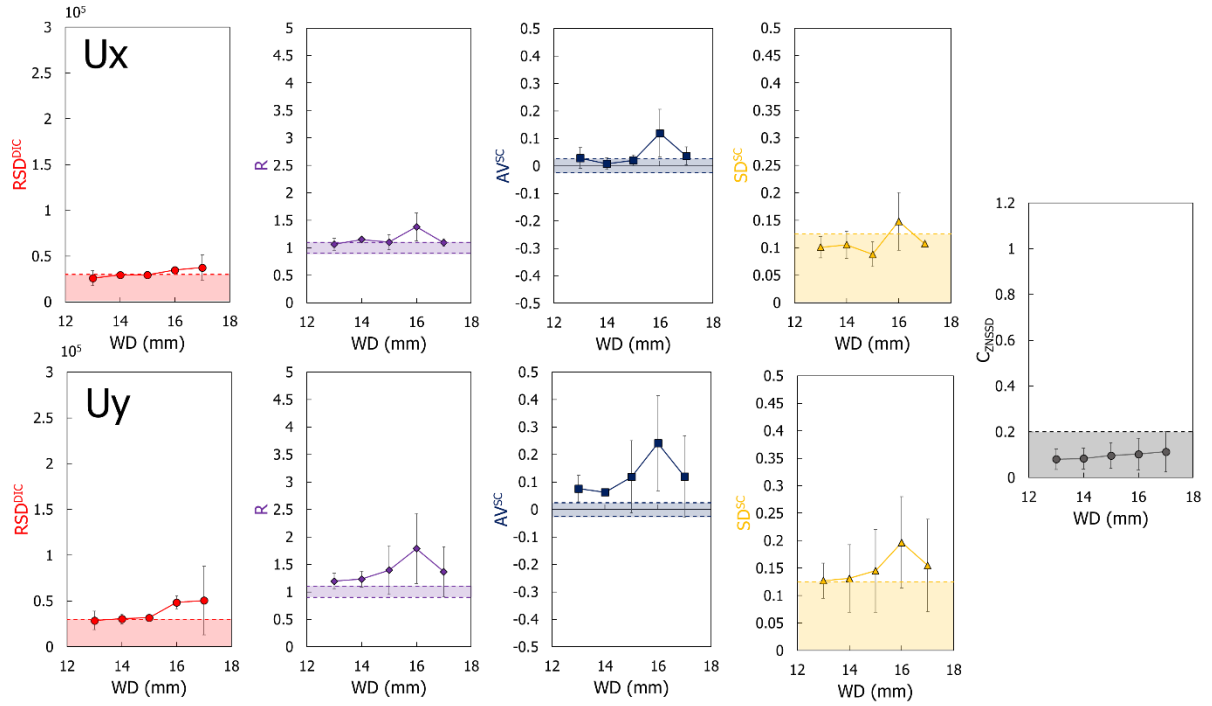


**Figure 7.** Evolution of statistical parameters as a function of working distance. Acceleration voltage: 10 kV, probe current number: 9, image size 1280×1056 pixels, integration: yes, number of frames: 4, scan time number: 5, mode: SE, magnification: ×1500. The colored area corresponds to the range of validity of each parameter defined in Table 2.



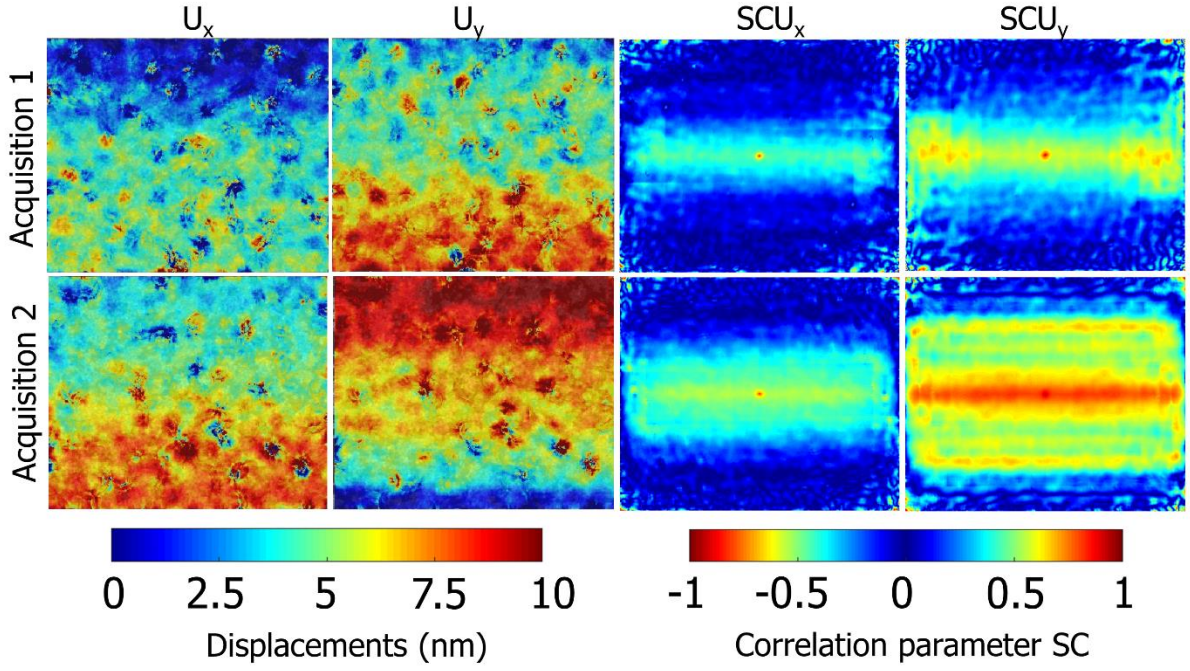


*Figure 8. Comparison of displacement and auto-correlation maps for two acquisitions performed under the same acquisition conditions (working distance = 16 mm). Acceleration voltage: 10 kV, probe current number: 9, working distance: 16 mm, image size 1280×1056 pixels, integration: yes, number of frames: 4, scan time number: 5, mode: SE, magnification: ×1500.*

The influence of the size of the images is now being investigated. The images were acquired at a magnification fixed at ×1500. At first, the images were not integrated. A scan time equal to 5 (dwell time of 2.89 μs) has been chosen in agreement with the best results obtained in Figure 5. The radius of the subset  $R_s$  was chosen so that it corresponds to a "physical" size of 1.9 μm for all the images (Figure 9). The correlation coefficient  $C_{ZNSD}$  is constant and not included in the fixed interval. This result usually indicates the presence of noise between the two images. For such large values of  $C_{ZNSD}$  it is generally observed that the statistical parameters  $R$ ,  $AV^{SC}$  and  $SD^{SC}$  are close to 1, 0 and 0.05 respectively. Under these conditions, the results of these statistical parameters are not very usable because the scan line shift and drift distortion artefacts are masked by the presence of noise in the image. In the case of Figure 9 large variations are obtained for the statistical parameters  $R$ ,  $AV^{SC}$ ,  $SD^{SC}$  and  $RSD^{DIC}$  indicating the significant presence of non-noise artefacts. Note also that the standard deviations associated with all the statistical parameters are very high, indicating poor repeatability of the acquisitions.

The visualization of the displacement and auto-correlation maps for the image with a resolution of 15.6 nm/pixel (5120×3840 pixels) shows that the measurement artifact obtained is of the line shift type, both on the rows and on the columns (Figure 10). Line shifts are even strongly observed, indicating a bad repositioning of the beam at the beginning of the line. The displacement field variations in the images are significantly larger than those observed



in the case where the images have a resolution of 62.5 nm/pixel (1280×1056 pixels) (20 nm vs. 3 nm for  $U_x$  displacement fields and 20 nm vs. 5 nm for  $U_y$  displacement fields). Since the line shift artifact is random, a possible solution to improve the stability of the images under the same conditions is to integrate the images. Tests were carried out in this sense by integrating the images: 2, 4 and 8 times. For an 8 times integrated images, a major decrease in the residual displacements in the images is observed (Figure 10). The amplitude decreases from 20 nm to 3 nm for the  $U_x$  displacement fields and from 10 nm to 7.5 nm for the  $U_y$  displacement fields.

The results obtained for the standard deviations of the displacements are presented in Table 3. A noticeable decrease is observed when the number of integrated images increases. However, it remains above the ranges fixed in Table 2. Since the number of random artifacts is greater for larger images, a higher number of integrated images would be required to drastically limit the presence of artifacts and obtain results similar to 1280×1056 pixel images.

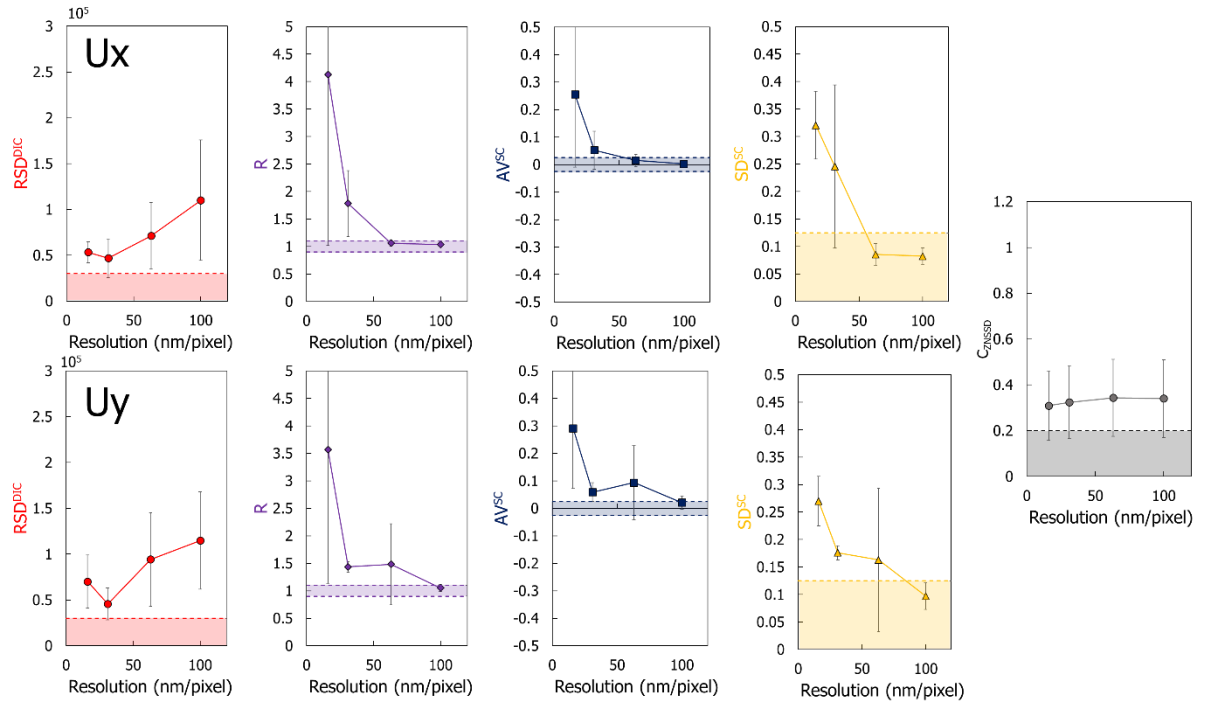


**Figure 9.** Evolution of statistical parameters as a function of resolution, same magnification (×1500). Acceleration voltage: 10 kV, probe current number: 9, working distance: 13 mm, integration: no, scan time number: 5, mode: SE. The colored area corresponds to the range of validity of each parameter defined in Table 2.

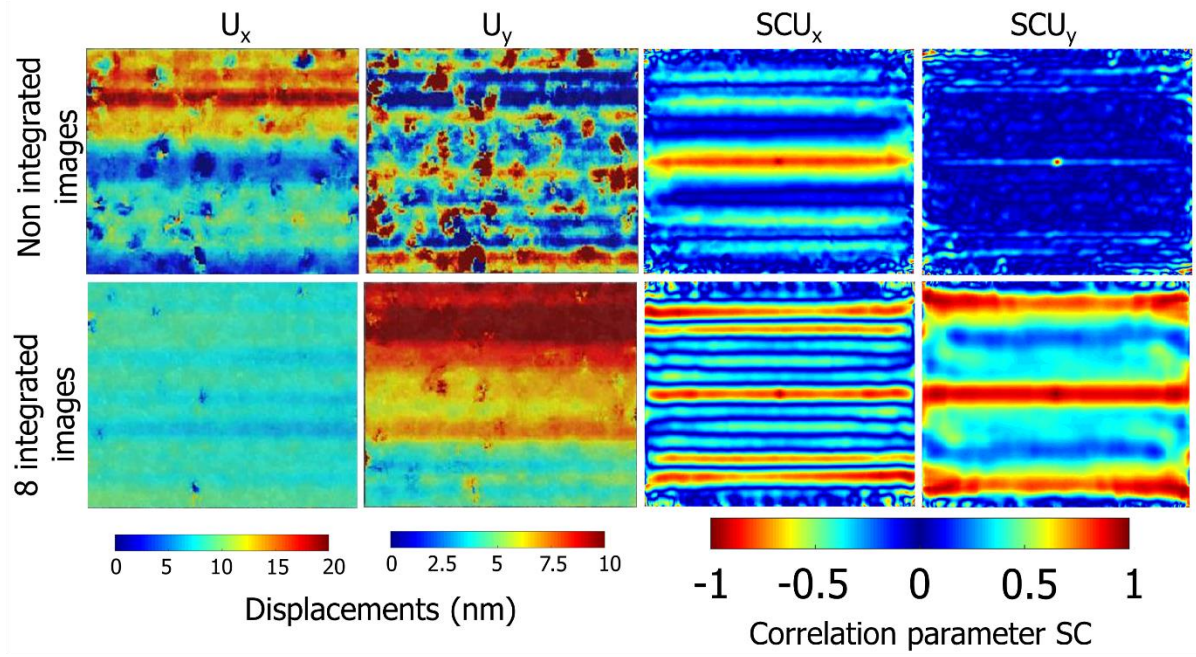


**Figure 10.** Comparison of displacement and auto-correlation maps for two not integrated images and 8 integrated images. Image size was set to 5120×3840 pixels. Acceleration voltage: 10 kV, probe current number: 9, working distance: 13 mm, scan time number: 5, mode: SE, magnification: ×1500.

	$RSD_{U_x}^{DIC} (10^5)$	$RSD_{U_y}^{DIC} (10^5)$
Non-integrated image	4.5	5.1
2 integrated images	2.9	3.3
4 integrated images	2.8	2.9
8 integrated images	0.8	1.8

**Table 3.** Evolution of relative standard deviation of displacements  $RSD^{DIC}$  in function of number of integrated images. Acceleration voltage: 10 kV, probe current number: 9, working distance: 13 mm, image size 5120×3840 pixels, scan time number: 5, mode: SE, magnification: ×1500.

Figure 11 shows the influence of the magnification (represented as a resolution) on the statistical parameters. The radius of the subset  $R_s$  is chosen so that it corresponds to a "physical" size of 1.9  $\mu\text{m}$  for the three magnifications. It appears that in the range of the investigated magnifications and for the selected analysis conditions, the impact of the magnification is low on the results. For a given resolution, it is therefore preferable to work at high magnification with small images (1280×1056 pixels) rather than working at low magnification with large images (5210×3840 pixels). On the other hand, the field of view will be strongly reduced.

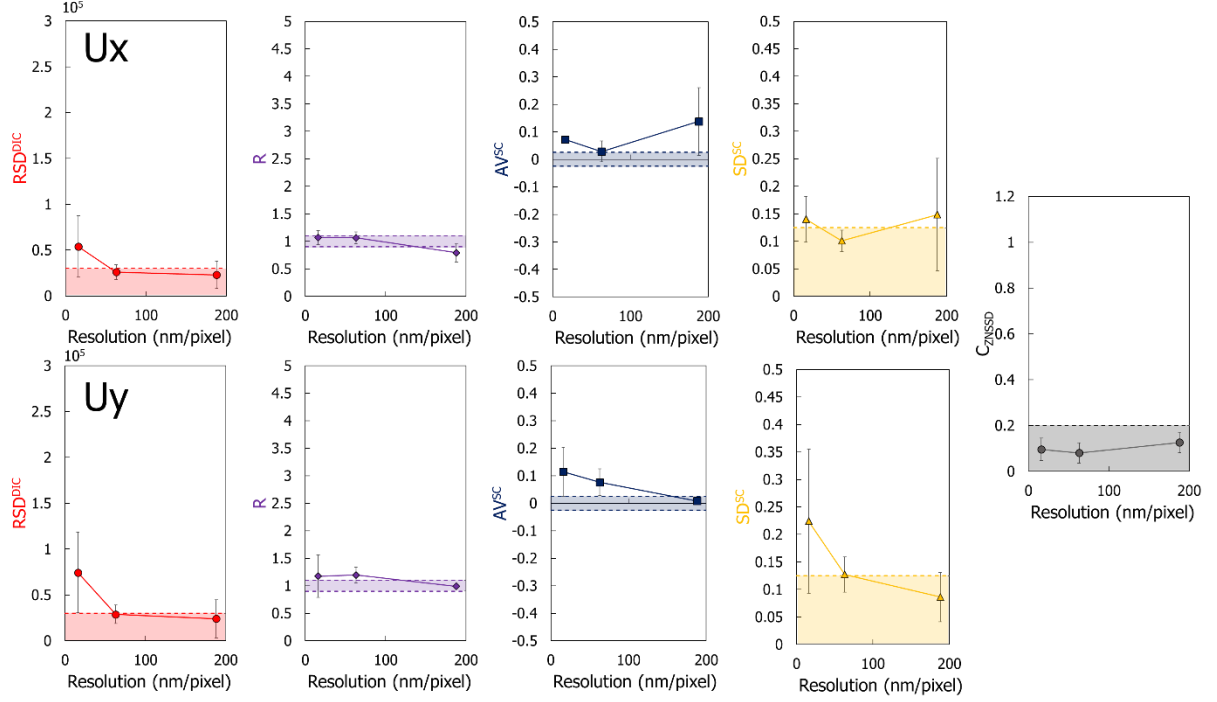


**Figure 11.** Evolution of statistical parameters as a function of resolution, identical image size  $1280 \times 1056$  pixels (subset radius depending on the resolution, "physical" value identical and equal to  $1.9 \mu\text{m}$ ). Acceleration voltage: 10 kV, probe current number: 9, working distance: 13 mm, integration: yes, number of frames: 4, scan time number: 5, mode: SE. The colored area corresponds to the range of validity of each parameter defined in Table 2.

## IV. Discussions

### IV. 1. Analysis of statistical parameters

A repeatability study was conducted by comparing the statistical parameters with the acquisition conditions outlined in Table 1. For all the images, the correlation coefficient is within the range to ensure a good correlation and possible interpretation of the results. The values of the statistical parameters  $RSD^{DIC}$ ,  $R$ ,  $SD^{SC}$ ,  $AV^{SC}$  are shown in Figure 12 as a function of the direction of the displacement fields. Two main pieces of information can be drawn from this figure: (i) the statistical parameters  $R$  and  $AV^{SC}$  show significant variations for the same acquisition conditions, while the parameters  $RSD^{DIC}$  and  $SD^{SC}$  are not very dependent on the direction of the displacement fields, (ii) the highest variations are obtained for the displacement field  $Uy$ .

(i) In order to identify the reason for these results, the impact of four temporal parameters was investigated: the time between the application of vacuum to the sample and the acquisition of the images, the time between two acquisitions, the time remaining at the same location (to see the effects of possible charging), and the time  $TvI$  between the opening of the airlock valve allowing the beam to reach the sample and the acquisition. Only the temporal parameters that had the greatest impact on the results are presented in the following ( $TvI$ ). From this

study, a link between  $TvI$  and the evolution of statistical parameters was obtained (Figure 13). An increase in  $TvI$  leads to an improvement in image stability. To illustrate this, Figure 14 shows the displacement and autocorrelation maps for different  $TvI$  times. For times less than 300 seconds, strong displacements  $U_y$  are obtained. A band characteristic of a continuous evolution in the image is observed for the  $SCU_y$  autocorrelation mappings. Weaker displacements are also observed along the  $x$ -axis. These different maps are characteristic of the presence of drift distortion of the beam. We recall that the drift distortion is the consequence of an unwanted movement of the specimen relative to the electron beam while the image is being taken. This artifact is not uniform in each image and varies from one image to another with time in a non-linear way. When  $TvI$  is too low, the artifact is present. It is therefore recommended to wait at least 1000 seconds between the moment when the airlock valve is opened and the taking of images in order to allow the beam to stabilize. Several investigations were conducted to explain these results. The vacuum value inside the chamber has been checked and does not indicate any variation between the images. Two hypotheses are therefore considered. The first concerns the electronics of the SEM detectors. A stabilization time would be necessary after being on standby. The second one concerns the possible influence of the charging effects of the sample. The use of alumina as a speckle on the surface of the sample induces an isolation of the sample. This could generate instabilities like those encountered at the beginning of the electron exposure. Further investigations would nevertheless be necessary to verify these hypotheses.

(ii) The scan line shift and beam distortion artifacts have the particularity of generating displacements preferentially in the  $y$  direction. They are particularly visible on the maps of the  $U_y$  displacement fields and therefore for the statistical parameters  $R_{U_y}$  and  $AV_{U_y}^{SC}$ . The fact that the statistical parameters for the  $U_y$  displacement fields are of lesser quality confirms that it is possible to detect these two artifacts with the methodology used.

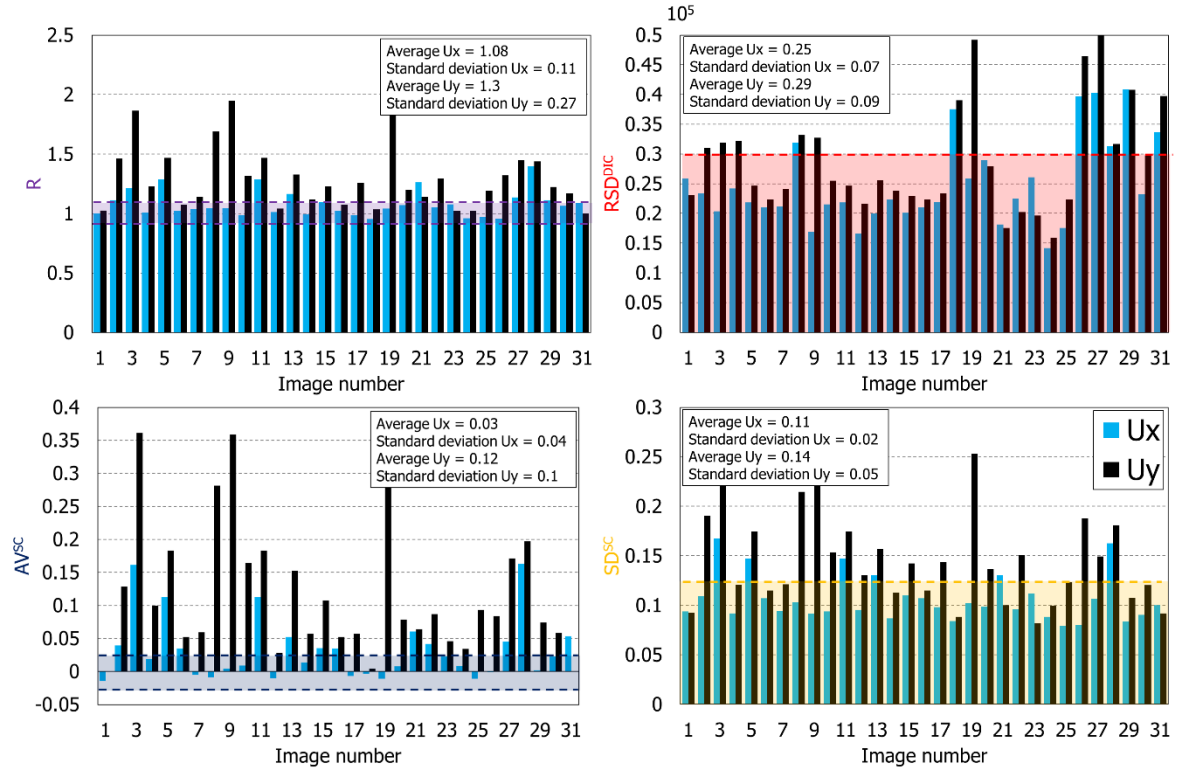


**Figure 12.** Influence of displacement field orientation on statistical parameters. Acceleration voltage: 10 kV, probe current number: 9, working distance: 13 mm, image size 1280×1056 pixels, integration: yes, number of frames: 4, scan time number: 5, mode: SE, magnification: ×1500. The colored area corresponds to the range of validity of each parameter defined in Table 2.

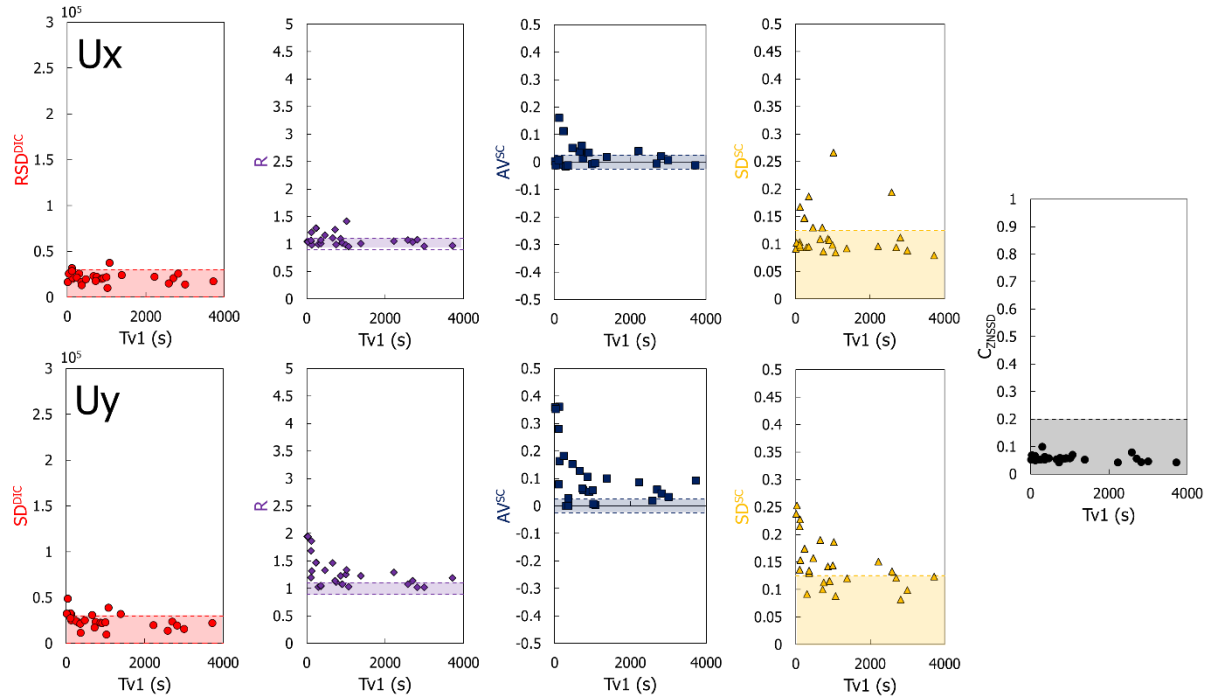


**Figure 13.** Evolution of the statistical parameters as a function of time after opening the airlock valve. Acceleration voltage: 10 kV, probe current number: 9, working distance: 13 mm, image size 1280×1056 pixels, integration: yes, number of frames: 4, scan time number: 5, mode: SE, magnification: ×1500. The colored area corresponds to the range of validity of each parameter defined in Table 2.



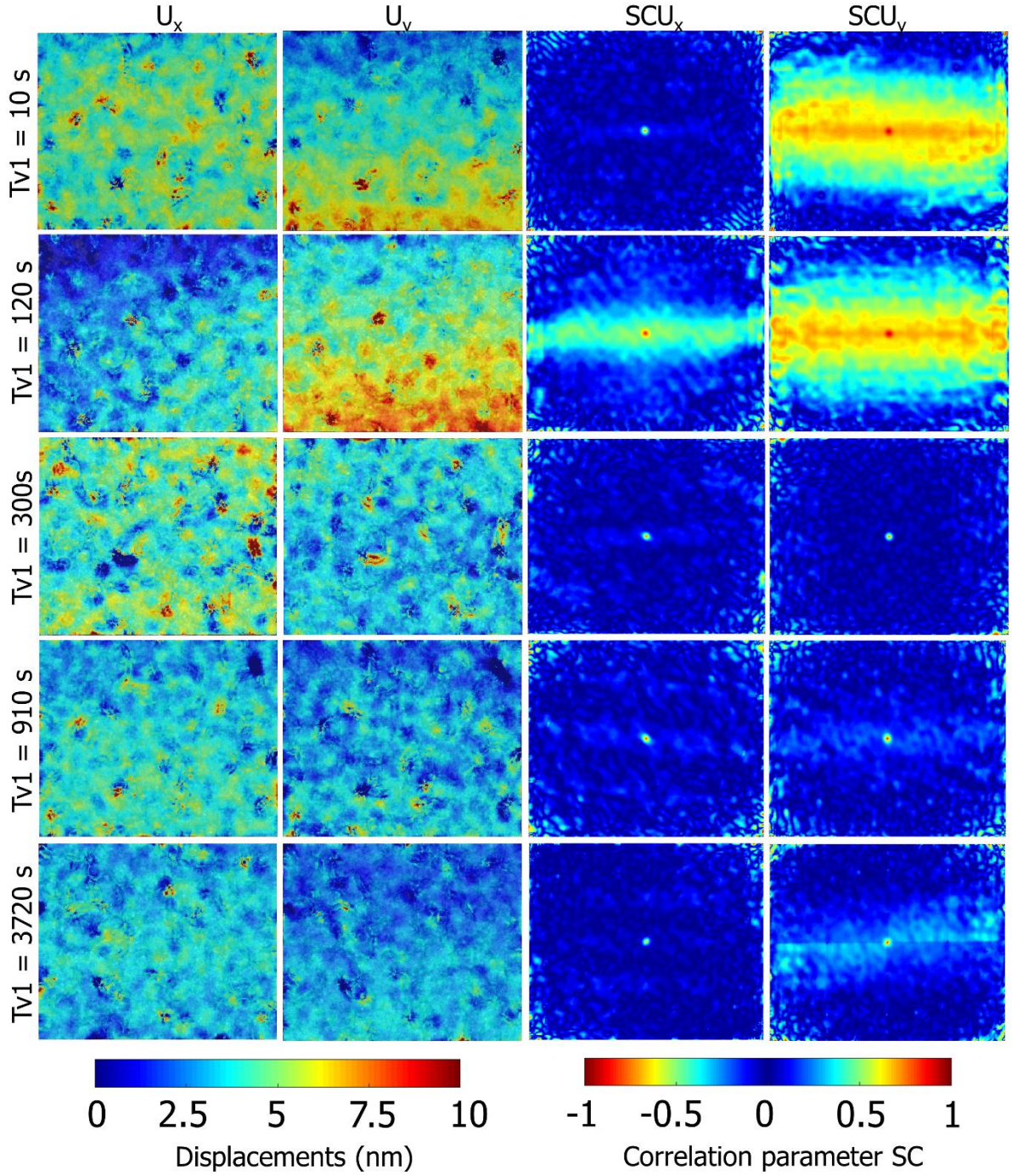


*Figure 14. Comparison of displacement and auto-correlation maps for five acquisitions performed under the same conditions, except for the time  $Tv1$  after opening the airlock valve. Acceleration voltage: 10 kV, probe current number: 9, working distance: 13 mm, image size 1280×1056 pixels, integration: yes, number of frames: 4, scan time number: 5, mode: SE, magnification: ×1500.*

Figure 15 shows a graph expressing the relationship between the statistical parameters  $R$  and  $AV^{SC}$  for all the images investigated. The red zone groups the acceptance interval of the images from these two parameters. A few images are contained in the area, showing the usefulness of the methodology. Characteristic groupings of images can be observed. The statistical parameter  $R$  is mostly greater than 1, showing that the artifacts are preferentially oriented along the lines. This could be characteristic of drift distortion and line shift artifacts. Some areas of the

graph have been flagged as characteristic of certain acquisition conditions. The symbols in the purple area ( $R < 1$ ) represent images that have the distinction of having been acquired immediately after inserting the sample into the SEM. In this case, unusual displacements in the  $x$  direction are visible on the maps. These artifacts are related to poor stabilization of the stage or the beam before acquisition. A waiting time of more than 300 seconds is recommended between the movement of the stage and the acquisition of images. The solid symbols located in the green zone represent the images having the particularity of having been acquired with a beam stabilization time of less than 1000 seconds. In this case, both parameters  $R_{uy}$  and  $AV_{uy}^{SC}$  are unusually high. Based on the previous observations, it was established that the relationship obtained in the green area between these two parameters is characteristic of a drift distortion artifact. Concerning the other, more scattered points, no particular type of artifact could be defined. On the other hand, this approach demonstrates that the use of a single parameter to qualify the quality of the images is insufficient. The use of this type of representation thus makes it possible to complete the analysis previously carried out.

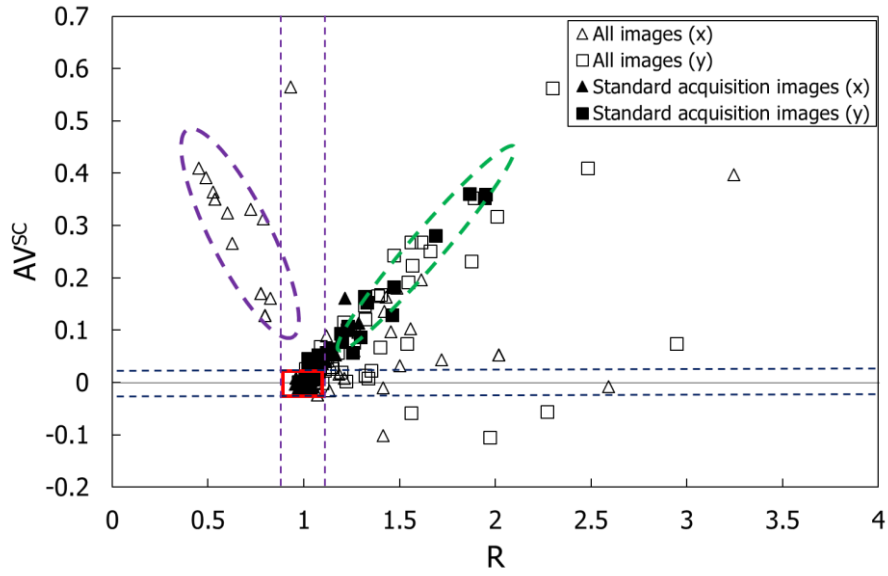


**Figure 15.** Relationship between the statistical parameters  $R$  and  $AV^{SC}$ .

#### IV. 2. Influence of speckle on statistical parameters

In order to identify the impact of speckle on the statistical parameters and the ability of the methodology to determine artifacts despite the use of a non-optimal speckle, a sensitivity study was conducted by varying the type of speckle used (Figure 16). Image 1, Figure 16.a, was acquired by an optical microscope with a speckle of lower density than the speckle used in the rest of this work. Image 2, Figure 16.b, corresponds to the image acquired with the SEM under standard conditions (Table 1). Image 3 and Image 4, Figure 16.c and Figure 16.d respectively, correspond to images created virtually according to the same methodology as used in [30]. The set of these images allows one to obtain a mean intensity gradient of the speckle pattern value ( $\delta_f$ ) ranging from 6.3 to 53.9. The gap in values between the four images can therefore clearly highlight the influence of speckle on the results. Moreover, virtual images allow for a homogeneously distributed speckle. The images have a size of 1000 pixels by 1000 pixels. A centered ROI whose size is 900×900 pixels was used for DIC.

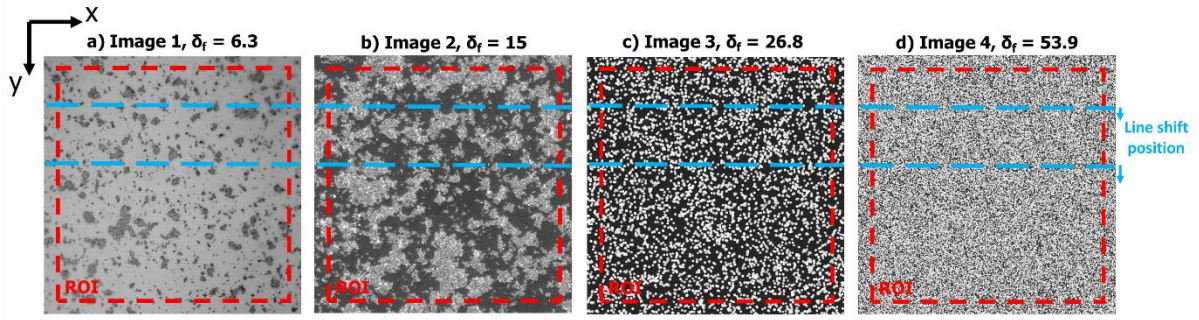


**Figure 16.** SEM image and virtual image used to evaluate the impact of the speckle on the statistical parameters.

Each of these images was distorted by introducing line shift artifacts. The artifacts were introduced as described in the following references [10], [12]. Two line shifts were introduced along the y-axis at values of  $y = 200$  pixels and  $y = 400$  pixels. The positioning of the line shift was chosen to be located in the least dense areas of image 2 in order to maximize the constraints related to the partial absence of speckle. The parameters used are presented in Table 4. Once the images were distorted, random noise was added following the same methodology as Goulmy *et al.* in order to reflect a random artifact. A normal law with a standard deviation of 15 greyscales was applied [30]. This step allows for a more accurate representation of reality, although the noise is voluntarily exaggerated here. Finally, the images were correlated using the same parameters as previously: a subset radius  $R_s$  was set to 30 pixels and a subset spacing was fixed at 2.

The results are presented as maps in Figure 17. The nature of the speckle has an impact on the results when the value of  $\delta_f$  is very low (of the order of 6 in the exposed case). Although degraded, the shape of the  $SCU_y$  maps is the same for all images, whatever the  $\delta_f$  value.



Variations are nevertheless observed and can be characterized when the evolution of statistical parameters is plotted as a function of the mean intensity gradient of the speckle pattern value (Figure 18). Since the artifact is oriented along the y-axis, the most notable variations are observed in the y-axis displacement mappings. It is then appropriate to discuss the influence of the speckle by studying mainly these mappings.

The  $\delta_f$  value has little impact on the statistical parameters  $AV^{SC}$ ,  $SD^{SC}$  and  $RSD^{DIC}$ . It also has little impact on the  $C_{ZNSSD}$  coefficient when the images are not noisy. On the other hand, in the presence of noise, the  $C_{ZNSSD}$  coefficient is greater than the value of  $\delta_f$  is low. Beyond a  $\delta_f$  value greater than 20, the impact of speckle becomes negligible, the  $C_{ZNSSD}$  coefficient does not change. Finally, the  $R$  parameter is strongly sensitive to the value of  $\delta_f$  and increases strongly when the latter increases.

The addition of noise leads to a decrease in the sensitivity of all statistical parameters, even when the correlation coefficient  $C_{ZNSSD}$  remains low. The impact of the presence of noise is greater when the value of  $\delta_f$  is low. We note, however, that the images used in the rest of this study ( $\delta_f > 15$ ) lead in all cases to values outside the specified tolerance intervals for the statistical parameters  $AV^{SC}$ ,  $SD^{SC}$ ,  $RSD^{DIC}$  and  $R$ . This study confirms the ability of the speckle used to detect measurement artifacts despite the fact that it has not been optimized. It should be noted that the optimization of the speckle can still lead to a greater sensitivity of the parameters (especially  $R$ ). This optimization could be achieved with the help of the gold remodeling method [31], sputter coating approaches [32], [33] or nanoparticle surface patterning [34].

Ax1	Ay1	Y01	W1	Ax2	Ay2	Y02	W2
0	0.05	200	1	0	0.12	400	1

**Table 4. Parameters of line shift artifact.**

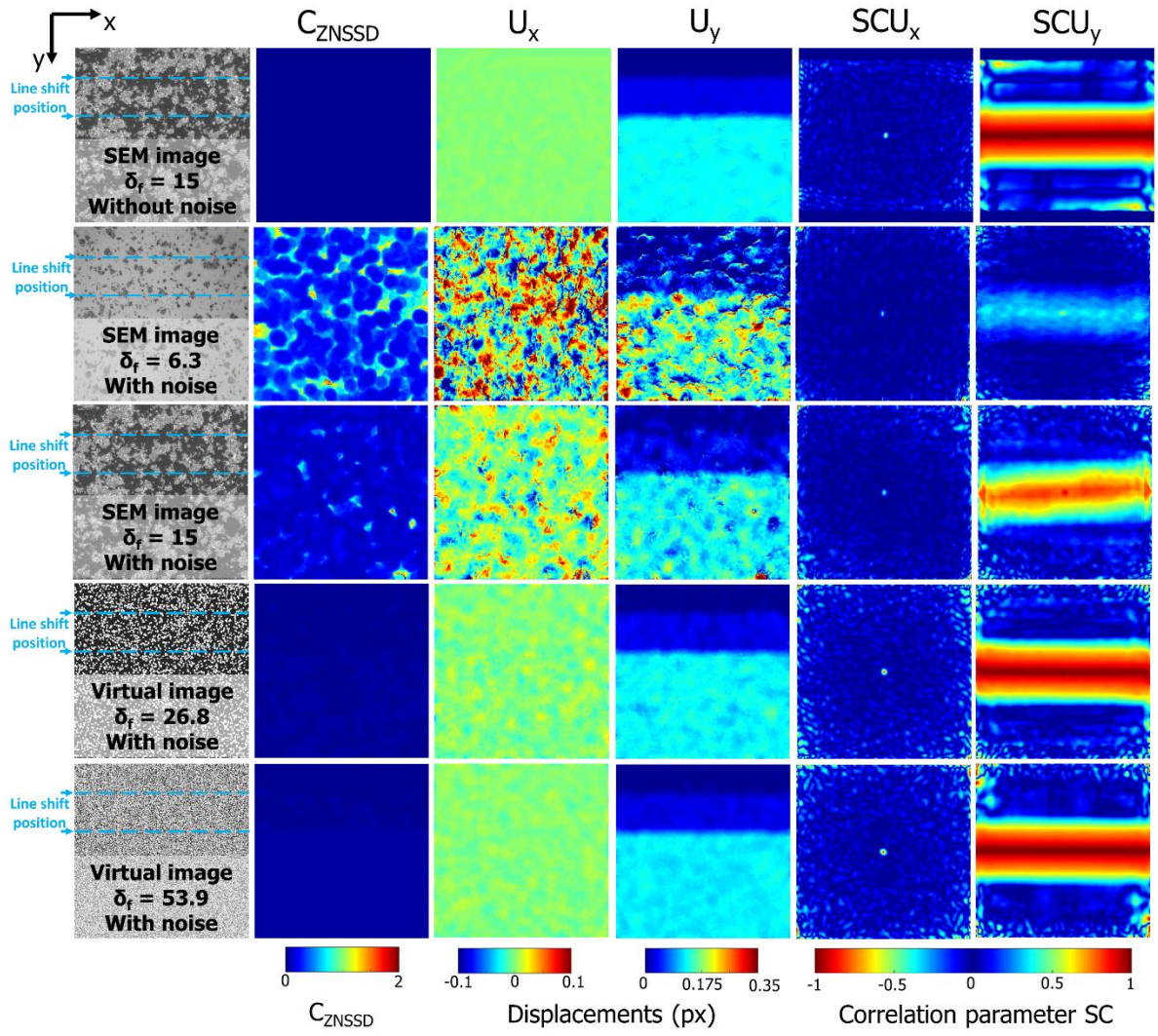
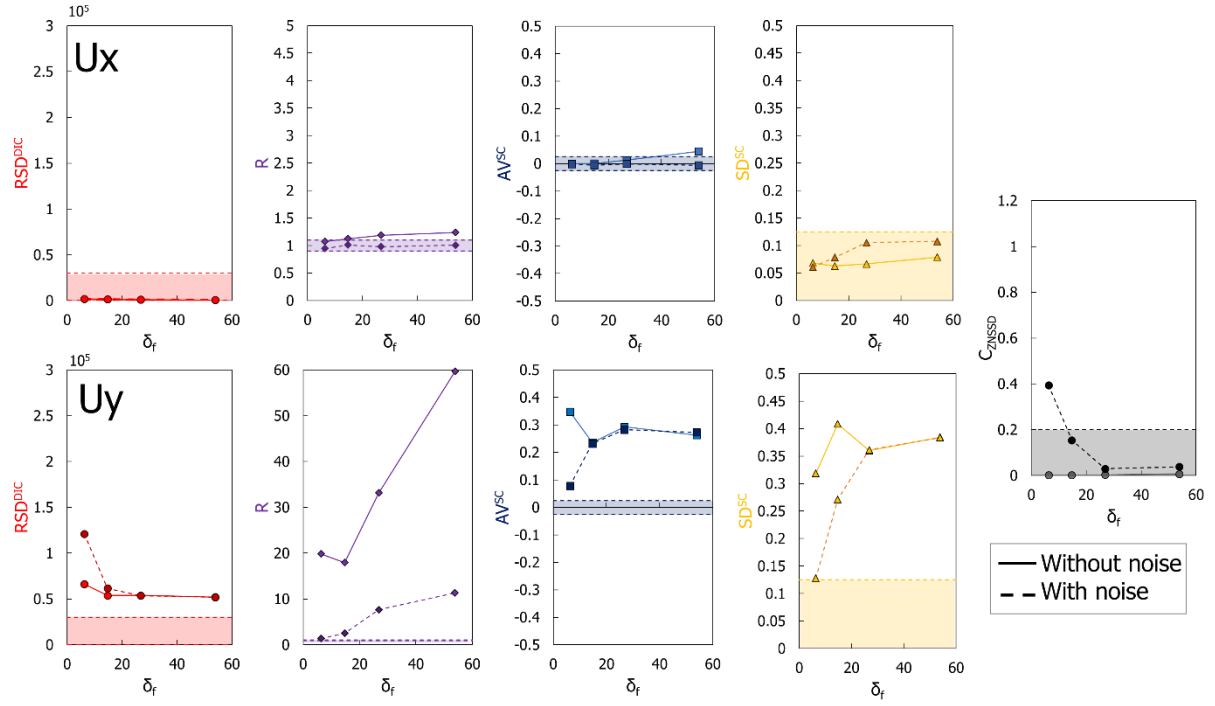


Figure 17. Comparison of  $C_{ZNSSD}$ , displacement, and auto-correlation maps for different kinds of speckle with two line shifts artifact.



**Figure 18.** Evolution of the statistical parameters as a function of  $\delta_f$ . The colored area corresponds to the range of validity of each parameter defined in Table 2.

#### IV. 3. Consideration of rastering artifact

The methodology used for all the results presented so far was to take two images in succession without applying a rigid body motion between the two images. Thus, the spatial artifact is not detectable [9]. Several methodologies can be used to take into account the spatial artifact [35], [36], [10]. They consist in applying rigid body translations to the specimen during a calibration step. Some images were acquired by translating the stage in the  $x$  and  $y$  directions following the same methodology as Maraghechi *et al.* [10]. Five successive images were taken under the same conditions. Image  $n^{\circ}1$  is taken at the same location as image  $n^{\circ}0$  which serves as a reference for the DIC (see in the upper right corner of Figure 19). Image  $n^{\circ}2$  is taken after a translation of the stage to the left of 100 pixels with respect to image  $n^{\circ}0$ . Image  $n^{\circ}3$  is acquired after a 100 pixels translation of the stage to the left and upwards with respect to image  $n^{\circ}0$ . Finally, image  $n^{\circ}4$  is acquired after a translation of the stage upwards of 100 pixels compared to image  $n^{\circ}0$ . The images then underwent the same processing as before and the statistical parameters were calculated. All images have a size of  $1280 \times 1056$  pixels. The selected ROI is the same for all the images. It was chosen to be contained in all the images. Its size is  $1080 \times 856$  pixels.

It has been reported in the literature that using a small working distance increases the presence of spatial artifact [18]. Therefore, measurements at working distances of 8 mm, 13 mm and 17 mm were performed. The

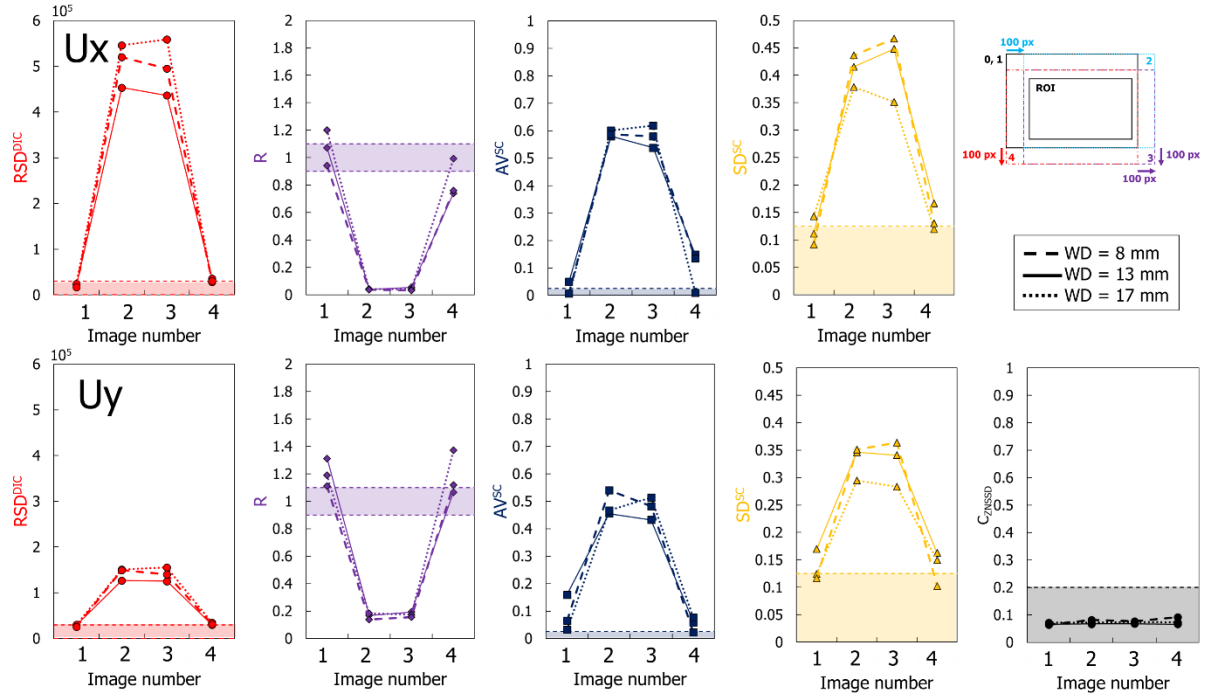
magnification was set at  $\times 1500$ . The results are shown in Figure 19. The evolution of the statistical parameters is similar whatever the working distance investigated is. Images n°2 and n°3 show a significant change in statistical parameters. Image n°4's evolution is more moderate when compared to image n°1. These results indicate that the artifact is mostly present when the stage is moved horizontally. Moreover, the position of the pixels in both directions is affected ( $U_x$  and  $U_y$ ). The statistical parameters evolve in the same way for both directions of the displacement fields. However, the magnitude of the evolution is smaller for the displacements obtained in the  $y$  direction. The ratio  $R$  being lower than 1, the observed artifact is mainly oriented along the  $x$  direction for the two displacement fields.

Figure 20 compares the displacement and auto-correlation maps after correlation of image n°0 with image n°2, for working distances of 8, 13 and 17 mm. To facilitate comparison of the displacement maps, all maps were reworked to impose a minimum calculated displacement value per map equal to 0 (rigid body motions have been removed from the maps). This representation allows a direct comparison of the artifact gradient generated at different working distances. A particular signature is obtained for the  $SC$  mappings, with wide vertical bands having values close to 1. Furthermore, observation of the displacement mappings indicates that the artifact is not centered and that a strong variation is obtained on the left side of the images, regardless of the observation direction ( $x$  or  $y$ ). A variation of nearly 300 nm is observed along the  $x$  direction, compared to 40 nm in the  $y$  direction. A key observation is that the artifact is not very dependent on the working distance.

Similar signatures concerning displacements have already been observed with less amplitude in the literature by Guo *et al.* [37]. Two types of distortion had been evoked to characterize these observations without it being possible to define which one was really present (drift or spatial artefact). If at first sight, the artifact observed here could be spatial, the independence of the artifact from the working distance seems to indicate that this is not the case [18]. It is more likely that it is an artifact related to the incorrect positioning of the beam on the left side of the image and therefore to the method of scanning the image (rastering type here). In view of these observations the artifact is relatively stable over time. This is why it is not detectable when two images are taken successively at the same location.

Additional, similar measurements were carried out at different day intervals. They showed that the artifact was indeed globally constant as long as a time of 1000 seconds after opening the airlock valve was respected. These observations can be directly linked to the observations made in Figure 15. In the case where the images are acquired for times less than 1000 seconds after opening the airlock valve, the artefact is not stable and there is a noticeable variation in the statistical parameters from one image to another, even though they were taken at the same location.

Although it is stable over time, as with the spatial artifact, rastering artifact must be taken into account during image acquisition. A calibration identical to that used to identify the spatial artifact can then be implemented [10]. Under the conditions used here, the rastering artifact has the greatest impact on the measurements compared to other possible artifacts.



**Figure 19.** Evolution of statistical parameters as a function of image number defined on the top right corner of the figure, working distance = 8, 13 and 17 mm. Acceleration voltage: 10 kV, probe current number: 9, image size 1280×1056 pixels, integration: yes, number of frames: 4, scan time number: 5, mode: SE, magnification: ×1500. The colored area corresponds to the range of validity of each parameter defined in Table 2. In the upper right corner: position of images in relation to each other.



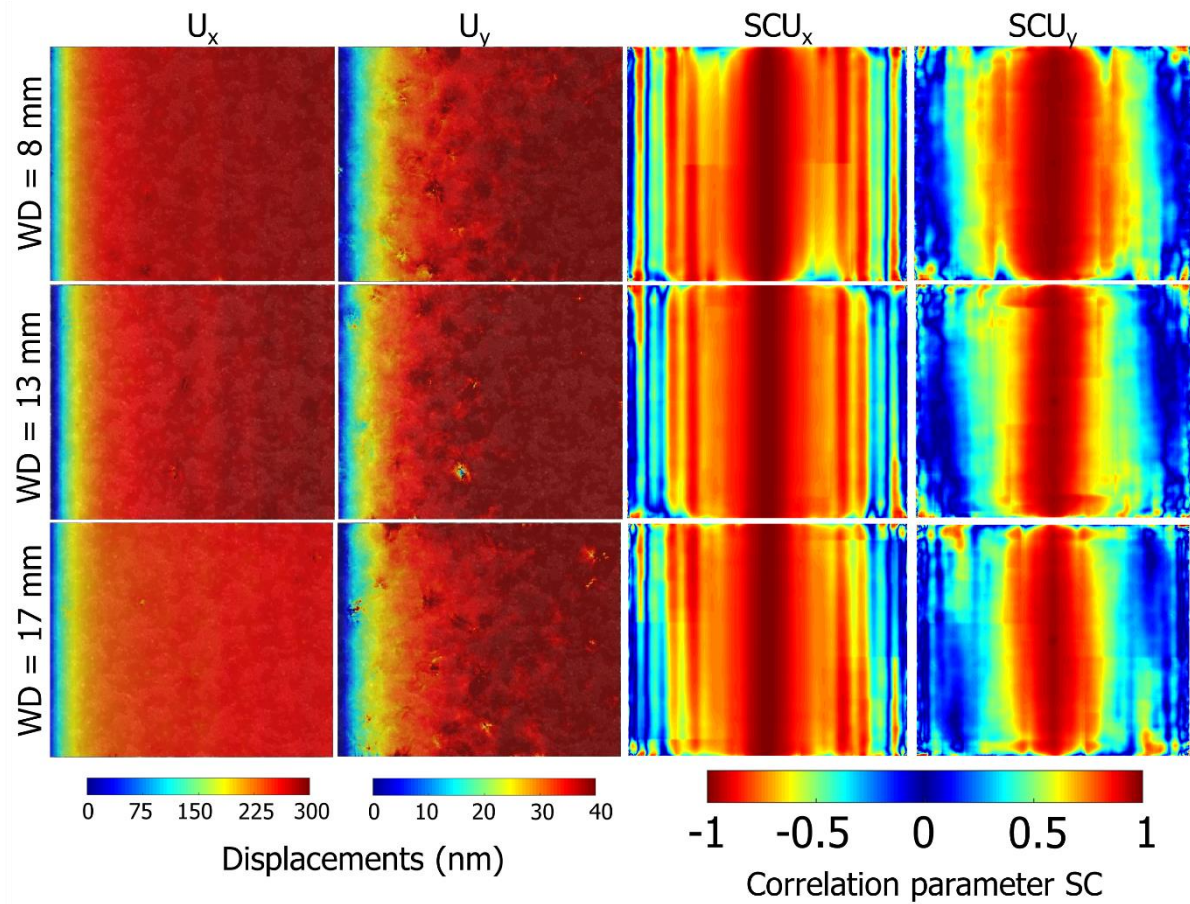


**Figure 20.** Comparison of displacement and auto-correlation mappings after correlation of image  $n^{\circ}0$  with image  $n^{\circ}2$ , for working distances of 8, 13 and 17 mm. Acceleration voltage: 10 kV, probe current number: 9, image size 1280×1056 pixels, integration: yes, number of frames: 4, scan time number: 5, mode: SE, magnification: ×1500.

#### IV. 4. Classification of acquisition parameters according to their degree of importance

The test matrix set up allowed us to classify the acquisition parameters of the SEM according to their influence on image stability (Table 5). The elements classified as "high importance" group together the parameters requiring particular attention in order to define the optimal conditions. The elements classified as "low importance" must be evaluated once the elements of "high importance" have been determined. The use of an average condition of these parameters gives satisfactory or even ideal results. Finally, parameters classified as "unimportant" have not been shown to have a major impact on the results when modified in a reasoned manner around a classically used value. They may not be tested to determine the optimal condition and an average condition is preferred.

High importance	Low importance	Little importance
<ul style="list-style-type: none"> <li>• Scanning speed</li> <li>• Integration</li> <li>• Number of integrated images</li> <li>• Image resolution</li> <li>• Time between the opening of the airlock valve and the taking of images</li> </ul>	<ul style="list-style-type: none"> <li>• Acceleration voltage</li> <li>• Working distance</li> <li>• Probe current</li> <li>• Magnification</li> </ul>	<ul style="list-style-type: none"> <li>• Contrast</li> <li>• Brightness</li> <li>• Exposure time of the sample in a given area</li> </ul>

*Table 5. Summary of the importance of the different SEM parameters on the stability of the images.*

The parameters that have a "strong importance" on image quality are: scan time, image integration, number of integrated images, image size, time from airlock valve opening to image capture, and subset size. The last parameter is independent of the SEM conditions but is nevertheless listed here because of the importance observed in this study. The scan time appeared to be one of the most important parameters to determine to improve the quality of the images. The influence of this parameter on the statistical parameters is high. It also induces dispersions between the statistical parameters, which makes the determination of this parameter a difficult choice. The best results are obtained for a scan time number of 5 (dwell time of 2.89  $\mu$ s), whether the images are integrated or not. A scan time that is too fast leads to an increase in image noise and poor image correlation, while a speed that is too slow leads to the presence of more artifacts such as beam drift distortion and line shift. The optimal condition is therefore the result of this compromise. It has been shown that the use of image integration is beneficial for all statistical parameters. On the other hand, the benefit is more or less marked depending on the scan time. The determination of the number of images to integrate results from a compromise between image quality and the time required to acquire the images. For images whose size is 1280×960 pixels, it has been shown that from 4 integrated images, the statistical parameters are contained in the defined interval. At the same time, the quality of the images does not appear to improve greatly beyond 8 images while the acquisition time evolves in a linear way. Thus, the optimal number of images to integrate is between 4 and 8. When the size of the images is increased, the presence of artifact is increased. Therefore, a number of integrated images would be necessary to improve image quality. Finally, one of the most important parameters for image quality is temporal. It has been shown that it is recommended to wait at least 1000 seconds between the moment when the airlock valve of the beam is opened and the capture of images. Several hypotheses have been put forward to explain these results (stabilization of the electronics, load effects), but further investigations would be necessary to be more accurate.

The parameters with a "low importance" on the quality of the images are: acceleration voltage, probe current, magnification and working distance. These four parameters are one of the main characteristics of SEMs and yet have little influence on the results. In the case of this work, it appeared that the most adequate condition was a voltage of 10 kV, even if the other two conditions did not induce poor quality images. Also, the optimal conditions

of measurement are located at values of probe current number of 8 or 9. Average values were therefore retained for these two parameters. To explain the weak influence of these two parameters on the statistical parameters, it is necessary to recall that when the influence of a parameter is studied, the conditions of the other parameters are fixed at an average value. For example, a low voltage with a high current has not been investigated, possibly masking the effects of these parameters on image quality. The magnification also has little impact on the stability of the images. The choice must therefore be made between the desired resolution and field of view. Finally, the working distance was set at a minimum value of 13 mm due to the measurement conditions imposed by the characteristics of the mechanical test stage. The investigation interval was therefore selected from 13 mm to 17 mm, showing no impact of the working distance on the quality of the images.

The parameters that do not have an impact on the stability of the images are: brightness, contrast and irradiation time of the sample. Also, the acquisition time is not a dimensioning parameter to define the quality of the images, but it has been observed that a value greater than 50 seconds is imperative to obtain stable images. Finally, the optimal acquisition conditions to limit the presence of line shift, drift distortion and noise artifacts are presented in Table 6.

Note that the selected acquisition conditions make it difficult to acquire very large fields of view. For example, to obtain a field of view and a resolution similar to Chen *et al.* [38] (5.5 mm  $\times$  3.4 mm), a total of 1960 images would be necessary, which would induce an acquisition time of 17 hours compared to only 3 hours for the authors previously cited (4096  $\times$  4096 images with a dwell time of 3.2  $\mu$ s). The selected acquisition conditions must therefore result from a compromise between the limitation of measurement artifacts and the acquisition time required to produce the images. The methodology presented here can therefore be used to achieve this compromise.

Acceleration voltage (kV)	Probe current number	Objective lens aperture	Working distance (mm)	Image size (px <sup>2</sup> )	Integration	Number of frames	Scan time number	Dwell time ( $\mu$ s)	Mode	Resolution (nm/pixel)
10	9	3 (50 $\mu$ m)	13	1280 $\times$ 1056	yes	8	5	2.89	SE	63

**Table 6. SEM conditions that will be used to perform mechanical tests.**

The methodology applied helps to distinguish the presence of the four types of artifacts commonly observed in the literature: noise, line shift, drift distortion and spatial distortion. The following recommendations can be made for effective implementation. In order to identify the presence of artifacts, a sufficiently large DIC subset size should be chosen to limit the measurement noise on the results. The first parameter to consider when analyzing image stability is the  $C_{ZSSD}$  coefficient. If it is greater than 0.2, the stability of the images cannot be commented on with respect to the other statistical parameters. Then, the  $AV^{SC}$  parameter is the most sensitive to identify the presence of artifacts. It must therefore be studied as a priority. The  $R$  parameter is particularly useful for identifying stage



movements or beam defects during acquisition. A  $R_{U_x}$  value lower than 1 is particularly suspicious and is characteristic of an unusual motion of the stage or the beam during the acquisition. In the absence of oriented artifacts, the  $RSD^{DIC}$  standard deviation is the most suitable to define the quality of the acquisition performed. Finally, to define the optimal acquisition conditions, it is useful to couple two of the three statistical parameters  $AV^{SC}$ ,  $R$  or  $SD^{DC}$ . By following this path, it is possible to limit the presence of beam drift, line shift and noise artifacts in the images. However, it is not possible to remove the spatial distortion or rastering artifact. To identify their presence, it is necessary to apply a rigid body motion to the specimen. To distinguish whether it is a spatial or rastering artifact, a study at different working distances is necessary. Among all the artifacts that can be observed, the rastering artifact has the greatest impact on the results. However, it has the advantage of being fixed for given conditions (with the equipment used in this work). It should then be characterized using the aforementioned methodologies and directly integrated into the DIC calculations [12], [39].

#### IV. 5. Mechanical test application

In order to validate the acquisition conditions, a tensile test was performed using a Kammrath and Weiss 5 kN machine. The stress axis was oriented along the  $x$ -axis (horizontal) for all strain maps and images. As the methodology outlined here is not material- or speckle-dependent, the mechanical tests were purposely carried out by modifying these conditions. The material used for the validation was commercially pure copper (99.9%). Chemical etching was used to generate small markers that were between 100 and 200 nm in size, allowing the application of high-resolution DIC [30]. Image acquisition was performed at a magnification of  $\times 5000$  allowing a resolution of 19 nm px<sup>-1</sup>. In addition, the acquisition conditions applied to perform the tests were those defined in Table 6. As previously, the DIC was performed by using a subset radius  $R$ , set to 30 pixels. A subset spacing was fixed to 2 and the strain radius was fixed to 1.

The calibration of the rastering artifact was performed by applying rigid body displacements, as expressed in Figure 19, to samples obtained prior to the mechanical test campaign under identical conditions. It is therefore assumed that the rastering artifact is reproducible from one test campaign to another. Since it is constant over time, the rastering artifact was determined using the same methodology used by Maraghechi *et al.* to account for the spatial artifact [10]. As the presence of scan line shift and drift distortion artifacts is limited by the choice of acquisition conditions, they are not considered in the following. In the continuation, vectors with components along  $x$  and  $y$  are specified in bold in the text.

Let  $x_0$  and  $x_1$  be the actual positions of the sample material features measured from images 0 and 1. Let  $X_0$  and  $X_1$  be the positions of these material points in the image. Let  $U_1$  be the displacement field measured from the image correlation and  $\varphi$  the spatial artifact. It is possible to write:

$$x_0 = X_0 + \varphi(X_0) \quad \text{Eq. 9}$$

$$x_1 = X_1 + U_1 + \varphi(X_1 + U_1) \quad \text{Eq. 10}$$

From the observations made in Figure 19, the rastering artifact is significantly oriented along the  $x$ -axis. After several tests concerning the shape of the spatial artifact, a polynomial of degree 6 was chosen to describe the rastering artefact (Eq. 11) where  $a_i$  represents the coefficients to be identified for the two displacement directions  $U_x$  and  $U_y$  using the calibration step.

$$\varphi(x) = a_0 + a_1x + a_2x^2 + a_3x^3 + a_4x^4 + a_5x^5 + a_6x^6 \quad \text{Eq. 11}$$

Once the  $a_i$  coefficients were identified using the calibration procedure, the true displacements  $U_r$  could be calculated according to Eq. 11 and Eq. 12.

$$U_r = x_1 - x_0 \quad \text{Eq. 12}$$

$$U_r = X_1 + U_1 + \varphi(X_1 + U_1) - (X_0 + \varphi(X_0)) \quad \text{Eq. 13}$$

Two average strains were applied to the specimen during the mechanical test (0.4% and 4%). The obtained  $\varepsilon_{xx}$  strain mappings are shown in Figure 21 with and without taking into account the spatial artifact. Taking the rastering artifact into account greatly improves the quality of the results (especially on the left side of the mappings) for the lowest strain levels (step 1). However, the consideration of the artifact could be even better if a calibration is performed before the beginning of each experiment even though the conditions are strictly identical. The impact of the correction is more moderate for the highest levels (step 2). Also, it is remarkable that the acquisition conditions allow the visualization of strain heterogeneities in the grains from the lowest imposed strain levels. When the strain is increased, localization bands characteristic of the activation of slip systems appear in the grains. At 4% strain, no slip bands are visible in the SEM images. Therefore, the test was conducted at 15% axial strain in order to exacerbate the presence of slip bands and visualize them directly in the SEM images. The image obtained is presented in Figure 21 (bottom left). Some slip bands are clearly visible and detected by the DIC. They are highlighted by red arrows in Figure 21. These observations confirm the test conditions. Other localization bands are obtained by DIC without being directly visible on the SEM image. This result shows that the selected test conditions allow determining the localization of the smallest deformations and thus the interest of the high resolution DIC application. More information on the choice of image resolution and correlation parameters in order to visualize the location bands or to calculate average values in each grain is presented in [40].

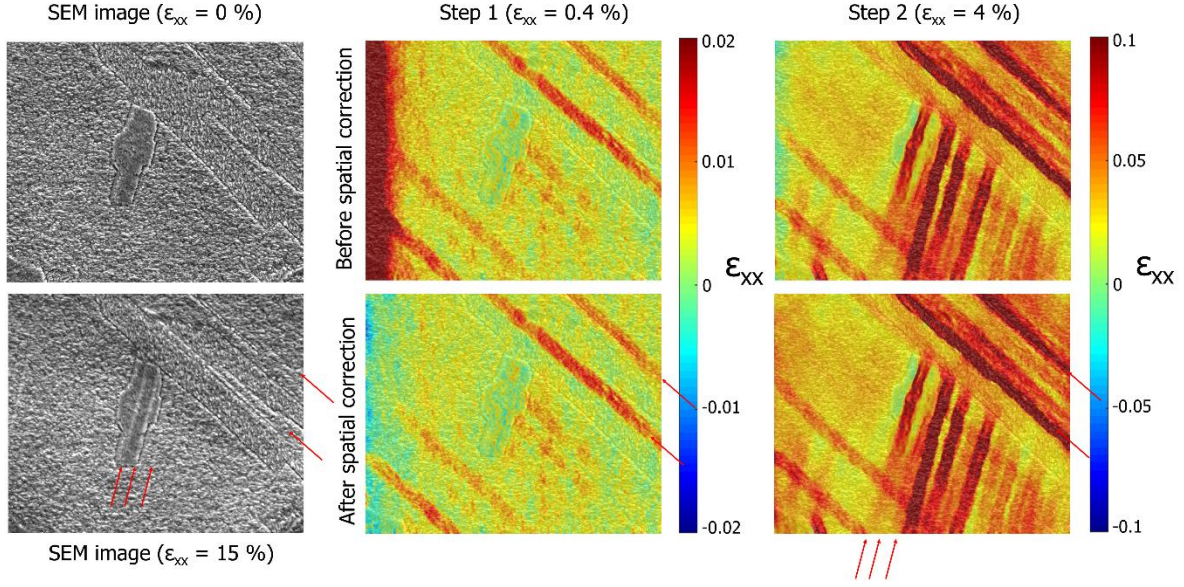


**Figure 21.**  $\epsilon_{xx}$  strain mappings with and without taking into account the rastering artifact for two strain levels. The red arrows represent the slip bands visible in the SEM images after 15% strain application and detected by DIC.

## V. Conclusion

Based on the study of statistical parameters, an extensive study was conducted to determine the influence of SEM acquisition parameters on the presence of measurement artifacts. This rigorous study allows one to classify the parameters according to their importance for the stability of the images when using high-resolution DIC. The parameters with the greatest influence on the occurrence of scan line shifts, drift distortions, and noise artifacts are: the dwell time, the number of integrated images, the image size, and the time between the opening of the airlock valve and the acquisition of the images. Therefore, these parameters must be changed as a priority when optimizing the acquisition conditions. On the other hand, the acceleration voltage, the probe current or the working distance did not seem to be the most important parameters. All the results were obtained with a single SEM. It would be interesting to check if similar trends are obtained for other SEMs following this same methodology. Some surprising results, such as those for the working distance of 16 mm, suggest that the methodology should be performed as soon as a new SEM device is used to better understand its specificities.

A link was established between the different statistical parameters to identify the origin of some measurement artifacts. In this way, it was possible to identify trends related to the waiting time after the displacement of the stage or the opening of the airlock valve. These new analyses lead to a better understanding of the influence of the different acquisition parameters on the results. They make it possible to propose an image acquisition protocol that limits the occurrence of measurement artifacts.

Although the influence of the size of the subset used in DIC is independent of the image acquisition, it seems to be an essential criterion for the detection of artifacts. Therefore, to perform the sensitivity study of the acquisition parameters, it is recommended to use a subset size similar to the one used in the analysis of the mechanical tests.

The implementation of the calibration methodology of the spatial artifact, classically used in the literature, coupled with the use of several working distances allowed us to highlight a rastering artifact rather than a spatial artifact. This artifact appeared to be constant even though the conditions of use of the equipment were modified. It can therefore be more easily taken into account when a calibration step is performed before the tests.

A mechanical test was finally performed on pure copper using the selected acquisition conditions. The rastering artifact was accounted for by performing a calibration step prior to testing. Since the rastering artifact is constant for given acquisition conditions, it has the greatest effect on the strain fields at the lowest strain levels. The ability of the methodology to perform mechanical tests under acquisition conditions that support visualization of strain heterogeneity while limiting the effects of acquisition conditions on measurements is thus demonstrated.

## VI. References

- [1] F. Lagattu, F. Bridier, P. Villechaise, and J. Brillaud, "In-plane strain measurements on a microscopic scale by coupling digital image correlation and an in situ SEM technique," *Materials Characterization*, vol. 56, no. 1, pp. 10–18, Jan. 2006, doi: 10.1016/j.matchar.2005.08.004.
- [2] F. Di Gioacchino and J. Quinta da Fonseca, "An experimental study of the polycrystalline plasticity of austenitic stainless steel," *International Journal of Plasticity*, vol. 74, pp. 92–109, Nov. 2015, doi: 10.1016/j.ijplas.2015.05.012.
- [3] J. C. Stinville, P. G. Callahan, M. A. Charpagne, M. P. Echlin, V. Valle, and T. M. Pollock, "Direct measurements of slip irreversibility in a nickel-based superalloy using high resolution digital image correlation," *Acta Materialia*, vol. 186, pp. 172–189, Mar. 2020, doi: 10.1016/j.actamat.2019.12.009.
- [4] H. W. Schreier and M. A. Sutton, "Systematic errors in digital image correlation due to undermatched subset shape functions," *Experimental Mechanics*, vol. 42, no. 3, pp. 303–310, Sep. 2002, doi: 10.1007/BF02410987.
- [5] F. Hild and S. Roux, "Digital Image Correlation: from Displacement Measurement to Identification of Elastic Properties – a Review," *Strain*, vol. 42, no. 2, pp. 69–80, 2006, doi: 10.1111/j.1475-1305.2006.00258.x.
- [6] D. Lecompte *et al.*, "Quality assessment of speckle patterns for digital image correlation," *Optics and Lasers in Engineering*, vol. 44, no. 11, pp. 1132–1145, Nov. 2006, doi: 10.1016/j.optlaseng.2005.10.004.
- [7] Y. Su, Q. Zhang, X. Xu, and Z. Gao, "Quality assessment of speckle patterns for DIC by consideration of both systematic errors and random errors," *Optics and Lasers in Engineering*, vol. 86, pp. 132–142, Nov. 2016, doi: 10.1016/j.optlaseng.2016.05.019.
- [8] C. Mansilla, V. Ocelík, and J. T. M. D. Hosson, "A New Methodology to Analyze Instabilities in SEM Imaging," *Microscopy and Microanalysis*, vol. 20, no. 6, pp. 1625–1637, Dec. 2014, doi: 10.1017/S1431927614013282.
- [9] M. A. Sutton *et al.*, "Scanning electron microscopy for quantitative small and large deformation measurements - part II: Experimental validation for magnifications from 200 to 10,000," *Experimental Mechanics*, vol. 47, no. 6, p. p.789-804, Dec. 2007, doi: 10.1007/s11340-007-9041-0.
- [10] S. Maraghechi, J. P. M. Hoefnagels, R. H. J. Peerlings, O. Rokoš, and M. G. D. Geers, "Correction of Scanning Electron Microscope Imaging Artifacts in a Novel Digital Image Correlation Framework," *Exp Mech*, vol. 59, no. 4, pp. 489–516, Apr. 2019, doi: 10.1007/s11340-018-00469-w.
- [11] M. T. Postek and A. E. Vladár, "Does your SEM Really tell the truth?-how would you know? Part 1: Does your SEM really tell the truth?," *SCA*, vol. 35, no. 6, pp. 355–361, Nov. 2013, doi: 10.1002/sca.21075.

- [12] S. Maraghechi, J. P. M. Hoefnagels, R. H. J. Peerlings, and M. G. D. Geers, "Correction of scan line shift artifacts in scanning electron microscopy: An extended digital image correlation framework," *Ultramicroscopy*, vol. 187, pp. 144–163, Apr. 2018, doi: 10.1016/j.ultramic.2018.01.002.
- [13] W. C. Lenthe, J. C. Stinville, M. P. Echlin, Z. Chen, S. Daly, and T. M. Pollock, "Advanced detector signal acquisition and electron beam scanning for high resolution SEM imaging," *Ultramicroscopy*, vol. 195, pp. 93–100, Dec. 2018, doi: 10.1016/j.ultramic.2018.08.025.
- [14] M. Haider, S. Uhlemann, and J. Zach, "Upper limits for the residual aberrations of a high-resolution aberration-corrected STEM," *Ultramicroscopy*, vol. 81, no. 3–4, pp. 163–175, Apr. 2000, doi: 10.1016/S0304-3991(99)00194-1.
- [15] C. Kisielowski *et al.*, "Detection of Single Atoms and Buried Defects in Three Dimensions by Aberration-Corrected Electron Microscope with 0.5-Å Information Limit," *Microscopy and Microanalysis*, vol. 14, no. 5, pp. 469–477, Oct. 2008, doi: 10.1017/S1431927608080902.
- [16] H. W. Schreier, D. Garcia, and M. A. Sutton, "Advances in light microscope stereo vision," *Experimental Mechanics*, vol. 44, no. 3, pp. 278–288, Jun. 2004, doi: 10.1007/BF02427894.
- [17] N. Cornille, "Accurate 3D shape and displacement measurement using a scanning electron microscope," PhD Thesis, 2005.
- [18] M. A. Sutton, N. Li, D. C. Joy, A. P. Reynolds, and X. Li, "Scanning Electron Microscopy for Quantitative Small and Large Deformation Measurements Part I: SEM Imaging at Magnifications from 200 to 10,000," *Exp Mech*, vol. 47, no. 6, pp. 775–787, Dec. 2007, doi: 10.1007/s11340-007-9042-z.
- [19] A. D. Kammers and S. H. Daly, "Digital Image Correlation under Scanning Electron Microscopy: Methodology and Validation," 2013, doi: 10.1007/s11340-013-9782-x.
- [20] B. Pan, Z. Lu, and H. Xie, "Mean intensity gradient: An effective global parameter for quality assessment of the speckle patterns used in digital image correlation," *Optics and Lasers in Engineering*, vol. 48, no. 4, pp. 469–477, Apr. 2010, doi: 10.1016/j.optlaseng.2009.08.010.
- [21] G. Crammond, S. W. Boyd, and J. M. Dulieu-Barton, "Speckle pattern quality assessment for digital image correlation," *Optics and Lasers in Engineering*, vol. 51, no. 12, pp. 1368–1378, Dec. 2013, doi: 10.1016/j.optlaseng.2013.03.014.
- [22] B. Pan, H. Xie, and Z. Wang, "Equivalence of digital image correlation criteria for pattern matching," *Applied optics*, vol. 49, pp. 5501–9, Oct. 2010, doi: 10.1364/AO.49.005501.
- [23] S. J. Orfanidis, *Optimum signal processing: an introduction*. Place of publication not identified: Sophocles J. Orfanidis, 2007.
- [24] N. Otsu, "A Threshold Selection Method from Gray-Level Histograms," *IEEE Transactions on Systems, Man, and Cybernetics*, vol. 9, no. 1, pp. 62–66, Jan. 1979, doi: 10.1109/TSMC.1979.4310076.
- [25] F. Brisset, M. Repoux, F. Robaut, and J. Ruste, *Microscopie électronique à balayage et microanalyses: en hommage à François Grillon*, Nouvelle éd. Les Ulis: EDP sciences, 2018.
- [26] Z. Chen, W. Lenthe, J. C. Stinville, M. Echlin, T. Pollock, and S. Daly, "High-Resolution Deformation Mapping Across Large Fields of View Using Scanning Electron Microscopy and Digital Image Correlation," *Experimental Mechanics*, vol. 58, pp. 1407–1421, 2018, doi: 10.1007/s11340-018-0419-y.
- [27] J. Blaber, B. Adair, and A. Antoniou, "Ncorr: Open-Source 2D Digital Image Correlation Matlab Software," *Exp Mech*, vol. 55, no. 6, pp. 1105–1122, Jul. 2015, doi: 10.1007/s11340-015-0009-1.
- [28] J. C. Stinville, P. Echlin, D. Texier, F. Bridier, P. Bocher, and T. M. Pollock, "Sub-grain scale digital image correlation by electron microscopy for polycrystalline materials during elastic and plastic deformation," *Experimental Mechanics*, vol. 56, no. 2, pp. 197–216, 2016, doi: 10.1007/s11340-015-0083-4.
- [29] J. S. Lyons, J. Liu, and M. A. Sutton, "High-temperature deformation measurements using digital-image correlation," *Experimental Mechanics*, vol. 36, no. 1, pp. 64–70, Mar. 1996, doi: 10.1007/BF02328699.
- [30] J. P. Goulmy, S. Jégou, and L. Barrallier, "Towards an image quality criterion to optimize Digital image correlation. Use of an analytical model to optimize acquisition conditions," *Optics & Laser Technology*, vol. 148, p. 107792, Apr. 2022, doi: 10.1016/j.optlastec.2021.107792.
- [31] F. Di Gioacchino, F. Da, and Q. J., "Plastic Strain Mapping with Sub-micron Resolution Using Digital Image Correlation," *Experimental Mechanics*, vol. 53, pp. 743–754, Jun. 2013, doi: 10.1007/s11340-012-9685-2.
- [32] J. P. M. Hoefnagels, M. P. F. H. L. van Maris, and T. Vermeij, "One-step deposition of nano-to-micron-scalable, high-quality digital image correlation patterns for high-strain *in-situ* multi-microscopy testing," *Strain*, vol. 55, no. 6, p. e12330, Dec. 2019, doi: 10.1111/str.12330.
- [33] C. B. Montgomery, B. Koohbor, and N. R. Sottos, "A Robust Patterning Technique for Electron Microscopy-Based Digital Image Correlation at Sub-Micron Resolutions," *Exp Mech*, vol. 59, no. 7, pp. 1063–1073, Sep. 2019, doi: 10.1007/s11340-019-00487-2.
- [34] A. D. Kammers and S. Daly, "Self-Assembled Nanoparticle Surface Patterning for Improved Digital Image Correlation in a Scanning Electron Microscope," *Exp Mech*, vol. 53, no. 8, pp. 1333–1341, Oct. 2013, doi: 10.1007/s11340-013-9734-5.

- [35] M. A. Sutton *et al.*, “Metrology in a scanning electron microscope: theoretical developments and experimental validation,” *Measurement Science and Technology*, vol. 17, no. 10, pp. 2613–2622, 2006, doi: 10.1088/0957-0233/17/10/012.
- [36] A. W. Mello, T. A. Book, A. Nicolas, S. E. Otto, C. J. Gilpin, and M. D. Sangid, “Distortion Correction Protocol for Digital Image Correlation after Scanning Electron Microscopy: Emphasis on Long Duration and Ex-Situ Experiments,” *Exp Mech*, vol. 57, no. 9, pp. 1395–1409, Nov. 2017, doi: 10.1007/s11340-017-0303-1.
- [37] Z. Chen, G. Fang, J. Xie, and J. Liang, “Experimental study of high-temperature tensile mechanical properties of 3D needled C/C–SiC composites,” *Materials Science and Engineering: A*, vol. 654, pp. 271–277, Jan. 2016, doi: 10.1016/j.msea.2015.12.010.
- [38] Z. Chen and S. Daly, “Automated identification of deformation twin systems in Mg WE43 from SEM DIC,” *Materials Characterization*, vol. 169, p. 110628, Nov. 2020, doi: 10.1016/j.matchar.2020.110628.
- [39] Q. Shi, S. Roux, F. Latourte, F. Hild, D. Loisonard, and N. Brynaert, “On the use of SEM correlative tools for in situ mechanical tests,” *Ultramicroscopy*, vol. 184, Part A, pp. 71–87, 2018, doi: 10.1016/j.ultramic.2017.08.005.
- [40] J. P. Goulmy, D. Depriester, F. Guittonneau, L. Barrallier, and S. Jégou, “Mechanical behavior of polycrystals: Coupled in situ DIC-EBSD analysis of pure copper under tensile test,” *Materials Characterization*, vol. 194, p. 112322, Dec. 2022, doi: 10.1016/j.matchar.2022.112322.